Research Square

Preprints are preliminary reports that have not undergone peer review.
They should not be considered conclusive, used to inform clinical practice,
or referenced by the media as validated information.

Eclipse-model sensitivity and numerical effects in orbit propagation

Minh Nguyen Cong

ncminh@vnu.edu.vn

Vietnam National University, Hanoi

Research Article

Keywords: solar radiation pressure, eclipse shadow factor, Encke method, oblate Earth, penumbra, equal-revolution benchmark, sensitivity analysis

Posted Date: September 22nd, 2026

DOI: https://doi.org/10.21203/rs.3.rs-11001857/v1

License: This work is licensed under a Creative Commons Attribution 4.0 International License.
Read Full License

Additional Declarations: No competing interests reported.

Eclipse-model sensitivity and numerical effects in orbit propagation

Cong Minh Nguyen*,[a]

[a] *VNU Hanoi – University of Engineering and Technology, 144 Xuan Thuy, Cau Giay, Hanoi, Vietnam*
*Corresponding author: Cong Minh Nguyen, Email: *ncminh@vnu.edu.vn*

Abstract

Differences between eclipse models do not translate directly into physical orbit corrections when shadow geometry, numerical evaluation, and propagation duration change together. This study develops a controlled comparison of these effects for initially circular Earth orbits under central gravity and cannonball solar radiation pressure. Four shadow formulations and supplementary temporal, matched-ray, solar-evolution, and horizon controls are evaluated on common nominal-period checkpoints. The comparison separates changes in the occulting limb from changes in its evaluation, and distinguishes stability of a model-pair difference from agreement of the individual trajectories. In 23 focused paired runs, event-split Encke propagation yields cylindrical-to-finite-Sun maxima of approximately 1.288 mm at 700 km and 1.064 m at 60000 km, compared with 3.807 mm and 1.782 m at the finest tested RK4 settings. The available LEO Cowell comparison changes the pair vector by 0.0237 mm while the individual trajectories change by about 18.6 mm. A separate equatorial matched-ray case exhibits a 0.0011 m change in the scalar maximum but a 0.0438 m change in its vector history, demonstrating why scalar agreement alone is insufficient. Frozen/moving-Sun and equal-period/equal-duration comparisons further expose the dependence on the prescribed experiment. Together, the results provide configuration-specific differential estimates and concrete counterexamples to interpreting production maxima as physical correction magnitudes. The contribution is an integrated set of attribution controls and quantitative diagnostics for eclipse-model comparisons; absolute orbit accuracy and general convergence of all surveyed configurations are not established.

Keywords: solar radiation pressure; eclipse shadow factor; Encke method; oblate Earth; penumbra; equal-revolution benchmark; sensitivity analysis

1. Introduction

Solar radiation pressure (SRP) connects spacecraft illumination with orbital evolution, so eclipse treatment influences both instantaneous forcing and its accumulated dynamical response. In the cannonball approximation, a shadow factor weights the incident momentum flux, making repeated ingress and egress passages relevant to long-arc propagation Montenbruck and Gill (2000); Valk and Lemaître (2008); Hubaux et al. (2012). Spacecraft geometry, surface properties, and attitude introduce further dependencies that are represented by analytical surface-force and navigation models Ziebart (2004); McMahon and Scheeres (2010). Adjustable box-wing and spacecraft-specific formulations account for these effects with different levels of physical detail Rodriguez-Solano et al. (2012); Bhattarai et al. (2019); Arnold et al. (2015). A useful comparison of eclipse prescriptions must therefore distinguish the response to illumination geometry from changes in the spacecraft model and numerical propagation.

The geometric and radiative ingredients of eclipse modelling are well established. Cylindrical and finite-Sun descriptions distinguish binary occultation from partial illumination, while oblate-Earth algorithms resolve the orientation-dependent terrestrial limb Ferraz Mello (1972); Adhya et al. (2004); Nugnes and Colombo (2023). Direct spherical/oblate and conical-shadow comparisons have been assessed against STK and telemetry for LEO satellites Srivastava et al. (2014, 2015). Atmospheric penumbra formulations additionally describe attenuation beyond the solid limb, including physically detailed treatments Li et al. (2019); Robertson et al. (2015); Robertson (2015). Building on these developments, the present question concerns what a propagated separation measures when changing a formulation also changes its numerical evaluation. Resolving that question requires controls that connect geometric model differences to the computed orbital response.

Previous dynamical and mission studies address important parts of that question. Hubaux et al. (2012) incorporated smooth shadow transitions into symplectic integration to control numerical energy drift, demonstrating that shadow treatment and propagation cannot be considered independently. Srivastava et al. (2021) combined orbit prediction and eclipse modelling for Chandrayaan-2 and compared the results with STK. Observation-based GPS, GLONASS, and BeiDou analyses assess radiation-force models within precise orbit determination Duan and Hugentobler (2021); Duan et al. (2020, 2022); BeiDou shadow comparisons and Galileo eclipse-period studies examine the consequences for those estimation settings Zhang et al. (2022); Chen et al. (2024). GRACE and Sentinel-6 MF validation likewise evaluates radiation-pressure modelling in a complete measurement-based context Vielberg et al. (2025). These studies motivate a complementary controlled experiment: their mission and integration results cannot by themselves assign a physical interpretation to a model-pair separation computed under a different, idealized force model.

Three connected attribution issues define the scope of the present comparison. First, replacing analytic spherical overlap by oblate-Earth ray integration changes both the limb and the evaluation procedure; a matched spherical-ray control is needed to distinguish those changes. Second, a binary eclipse switch can generate integration-dependent differences, and apparent agreement between two scalar maxima can conceal disagreement between the underlying vector histories. Stability of the difference between two model trajectories must also be distinguished from stability of each trajectory, because shared numerical displacement can cancel when the difference is formed. Third, equal nominal revolution counts represent unequal elapsed times across orbital regimes, while a frozen Sun preserves forcing geometry that an evolving solar direction does not. These issues call for a coordinated comparison of geometry, integration, and observation of the computed output, consistent with the distinction between numerical verification and physical validation Oberkampf and Roy (2010).

The methodological contribution is to bring these controls into one benchmark with unchanged spacecraft response, force assumptions, and initial-state conventions. Adjacent and cumulative differences are retained, but their interpretation is tested using common-checkpoint vector changes, matched spherical/oblate rays, and both equal-period and equal-duration horizons. A focused 23-run subset additionally compares event-split Encke results with RK4 refinement and an available independently stepped Cowell calculation. This design yields specific evidence for two distinct numerical effects: small scalar-maximum changes can coexist with large pair-vector changes, and small pair-vector changes can coexist with larger individual-trajectory changes. Their joint demonstration provides quantitative criteria for interpreting the sensitivity maps and for identifying which reported separations remain dependent on numerical implementation.

The study consequently asks which features of the sensitivity maps persist under the available

controls and which cannot yet be attributed to the shadow prescription alone. Four production sweeps vary area-to-mass ratio, inclination, altitude, and right ascension of the ascending node, while Cases 5–8 test resolution, solar evolution, propagation horizon, transmission height, and neighboring extrema. The results first connect local eclipse geometry to forcing, then evaluate long-arc numerical sensitivity before interpreting the parameter sweeps. The discussion combines the controls into guidance on what must accompany a reported model difference if that difference is to be scientifically interpretable. Complete supplementary records support reconstruction of the comparisons, while conclusions remain restricted to the tested differential response and do not imply observational accuracy or global convergence of the survey.

2. Methodology

2.1. Problem definition and reference geometry

All states are expressed in an Earth-centered inertial (ECI) frame whose z axis is aligned with the terrestrial polar axis. The spacecraft position and velocity are $\mathbf{r}$ and $\mathbf{v}$, the Earth-to-Sun vector is $\mathbf{r}_\odot$, and the spacecraft-to-Sun vector is

$$\mathbf{s} = \mathbf{r}_\odot - \mathbf{r}, \qquad s = \|\mathbf{s}\|. \tag{2.1}$$

The WGS-84 ellipsoid is represented by the equatorial semi-axis $a_E = 6378137$ m and flattening $f = 1/298.257223563$, with polar semi-axis

$$b_E = a_E(1 - f). \tag{2.2}$$

The gravitational parameter is $\mu_E = 3.986004418 \times 10^{14}$ m^3 s^{-2}. The implementation uses $R_\odot = 6.957 \times 10^8$ m and AU $= 1.495978707 \times 10^{11}$ m Prša et al. (2016); Vallado (2013). The altitude parameter is $h = a_0 - a_E$, referenced to the equatorial radius rather than local geodetic height.

Two fixed solar geometries are used for distinct parts of the benchmark. The original short-arc numerical verification uses 1 January 2025, 00:00 UTC ($JD_{\text{ver}} = 2460676.5$). The representative single-eclipse transition analysis and all production sensitivity sweeps use the near-equinox epoch 20 March 2025, 00:00 UTC ($JD_{\text{sens}} = 2460754.5$), selected to provide eclipse encounters across the prescribed orbital regimes under a common baseline orientation. For either epoch, the solar state is evaluated from the same low-precision approximate-Sun relations U.S. Naval Observatory (n.d.):

$$n_d = JD - 2451545.0, \tag{2.3}$$
$$L = \mathrm{mod}(280.460 + 0.9856474 n_d, 360^\circ), \tag{2.4}$$
$$g = \mathrm{mod}(357.528 + 0.9856003 n_d, 360^\circ), \tag{2.5}$$
$$\lambda = L + 1.915 \sin g + 0.020 \sin(2g), \tag{2.6}$$
$$\varepsilon = 23.439^\circ - 4.0 \times 10^{-7} n_d, \tag{2.7}$$
$$D_\odot/\mathrm{AU} = 1.00014 - 0.01671 \cos g - 0.00014 \cos(2g), \tag{2.8}$$

with

$$\hat{\mathbf{u}}_\odot = \begin{bmatrix} \cos\lambda & \sin\lambda \cos\varepsilon & \sin\lambda \sin\varepsilon \end{bmatrix}^T, \qquad \mathbf{r}_\odot = D_\odot \hat{\mathbf{u}}_\odot. \tag{2.9}$$

The Sun vector is fixed in Cases 1–6 and 8 and in the frozen-Sun branch of Case 7. The moving-Sun branch reevaluates Eqs. (2.8)–(2.9) at $JD(t) = JD_{\text{sens}} + t/86400$, with t in seconds. The coefficients printed here reproduce the MATLAB implementation; they are rounded variants of

the approximate relations documented by U.S. Naval Observatory (n.d.), not the exact coefficients currently listed there. Angles in Eq. (2.8) are in degrees. The resulting solar geometry is an idealized inertial prescription, not a precision ephemeris or a complete transformation between celestial reference frames.

All initial orbits are circular. With argument of latitude u_0, inclination i, RAAN Ω, and mean motion $n = \sqrt{\mu_E/a^3}$, the initial state is Vallado (2013); Curtis (2014)

$$\mathbf{r}_0 = a \begin{bmatrix} \cos\Omega\cos u_0 - \sin\Omega\sin u_0\cos i \\ \sin\Omega\cos u_0 + \cos\Omega\sin u_0\cos i \\ \sin u_0 \sin i \end{bmatrix}, \tag{2.10}$$

$$\mathbf{v}_0 = an \begin{bmatrix} -(\cos\Omega\sin u_0 + \sin\Omega\cos u_0\cos i) \\ -(\sin\Omega\sin u_0 - \cos\Omega\cos u_0\cos i) \\ \cos u_0 \sin i \end{bmatrix}. \tag{2.11}$$

For configurations with $\sin i = 0$, corresponding to $i = 0^\circ$ or 180°, the RAAN is not uniquely defined in the classical-element sense. In these endpoint geometries, the specified value $\Omega = 0^\circ$ is used only as a Cartesian-state orientation convention in Eqs. (2.10)–(2.11) and is not interpreted as a uniquely defined ascending-node direction.

2.2. SRP dynamics and Encke propagation

The dynamical model contains central Earth gravity and cannonball SRP,

$$\ddot{\mathbf{r}} = -\frac{\mu_E}{r^3}\mathbf{r} + \mathbf{a}_{\mathrm{SRP}}. \tag{2.12}$$

The restricted force model defines a controlled experiment. Forces common to all runs need not cancel from trajectory differences, because they alter the evolving orbit and eclipse geometry. Therefore, omitting additional perturbations restricts the domain of the conclusions rather than proving that their inclusion would be irrelevant. In particular, coupled SRP and gravitational oblateness admit structured phase-space and resonant dynamics Alessi et al. (2019); Gkolias et al. (2020). The oblate occulting surface used here does not introduce the gravitational J_2 term. Consequently, a peak in this benchmark is not evidence of one of those SRP–J_2 resonances.

The SRP acceleration is Musen (1960); Fliegel et al. (1992); Montenbruck and Gill (2000)

$$\mathbf{a}_{\mathrm{SRP}} = \nu P_0 C_R \frac{A}{m}\left(\frac{\mathrm{AU}}{s}\right)^2\left(-\frac{\mathbf{s}}{s}\right), \tag{2.13}$$

where $P_0 = 4.56 \times 10^{-6}$ N m^{-2} and $C_R = 1$ in the baseline cases. The shadow formulation therefore enters the common force model exclusively through ν. All shadow formulations retain the same optical coefficient and area-to-mass ratio within each paired run. This common response law makes illumination weighting the controlled difference in the prescribed acceleration.

Encke's method decomposes the perturbed state into a Keplerian reference state and a deviation Battin (1999); Curtis (2014):

$$\mathbf{r} = \mathbf{r}_{\mathrm{ref}} + \delta\mathbf{r}, \qquad \mathbf{v} = \mathbf{v}_{\mathrm{ref}} + \delta\mathbf{v}. \tag{2.14}$$

Subtracting the reference two-body equation from Eq. (2.12) gives

$$\ddot{\delta\mathbf{r}} = -\mu_E\left(\frac{\mathbf{r}}{r^3} - \frac{\mathbf{r}_{\mathrm{ref}}}{r_{\mathrm{ref}}^3}\right) + \mathbf{a}_{\mathrm{SRP}}. \tag{2.15}$$

For numerical evaluation, define the Encke parameter

$$q = \frac{\delta\mathbf{r} \cdot (2\mathbf{r} - \delta\mathbf{r})}{r^2} = 1 - \frac{r_{\mathrm{ref}}^2}{r^2}. \tag{2.16}$$

It follows that

$$F(q) = 1 - (1-q)^{3/2} = \frac{q(q^2 - 3q + 3)}{1 + (1-q)^{3/2}}. \tag{2.17}$$

The regularized Encke equation is therefore

$$\boxed{\ddot{\delta\mathbf{r}} = -\frac{\mu_E}{r_{\mathrm{ref}}^3}\left[\delta\mathbf{r} - F(q)\mathbf{r}\right] + \mathbf{a}_{\mathrm{SRP}}} \tag{2.18}$$

which is algebraically identical to Eq. (2.15). The identity follows directly from $(1-q)^{3/2} = r_{\mathrm{ref}}^3/r^3$. Equation (2.17) is evaluated in its rationalized form to avoid subtracting two nearly equal quantities when q is small.

The two-body reference orbit is evaluated with the universal-variable Kepler formulation and Stumpff functions Battin (1999); Curtis (2014). The deviation state is integrated with classical RK4 Hairer et al. (1993). The nominal step is

$$h_0 = \frac{T_0}{N_s}, \qquad T_0 = 2\pi\sqrt{\frac{a_0^3}{\mu_E}}, \tag{2.19}$$

with $N_s = 1200$ nominal steps per initial revolution in the production configuration. Because shadow-factor gradients are concentrated at eclipse boundaries, the step is locally reduced by a factor of eight within an angular neighborhood of the outer penumbra and inner umbra boundaries. Eclipse-local step refinement is consistent with the numerical requirement that penumbra transitions be resolved more finely than smooth orbital arcs Zhang et al. (2022). Output states remain constrained to the exact revolution checkpoints.

Rectification is applied when

$$\frac{\|\delta\mathbf{r}\|}{\|\mathbf{r}_{\mathrm{ref}}\|} > \epsilon_{\mathrm{rect}}, \qquad \epsilon_{\mathrm{rect}} = 10^{-3}, \tag{2.20}$$

after which the instantaneous perturbed state becomes the new Keplerian reference and the deviation is reset to zero. For the 50-period comparisons, the baseline output times are

$$t_N = NT_0, \qquad N = N_{\mathrm{orb}} = 0, 1, \ldots, 50. \tag{2.21}$$

Here, $N_{\mathrm{orb}} = t/T_0$ denotes a nominal revolution index based on the initial Keplerian period T_0. It is not obtained by geometrically detecting completed revolutions of the perturbed trajectory. Accordingly, $N_{\mathrm{orb}} = 50$ corresponds to 50 initial-orbit periods for each configuration, and the term "equal-revolution" is used throughout to denote comparisons performed at equal values of this nominal index.

2.3. Eclipse-model fidelity hierarchy

The hierarchy introduces finite solar extent, an oblate occulting limb, and prescribed transmission in succession (Table 1 and Fig. 1). M1–M2 also changes the evaluation from apparent-disc overlap to angular quadrature; Case 6 controls that change explicitly. Here, fidelity denotes added model structure, not an established ordering of physical accuracy. The cumulative M0–M3 comparison measures the response to traversing this complete sequence.

Table 1: Eclipse-model hierarchy and the physical/geometric increment introduced at each level.

Model	Finite-Sun treatment	Earth-limb treatment	Atmosphere treatment
M0	Point-source Sun	Spherical cylindrical shadow	None
M1	Analytic apparent-disc overlap	Spherical Earth	None
M2	Solar-disc quadrature	WGS-84 ray–ellipsoid intersection	None
M3	Same solar-disc quadrature	Same WGS-84 ellipsoid	Linear TOA transmission on limb-grazing rays

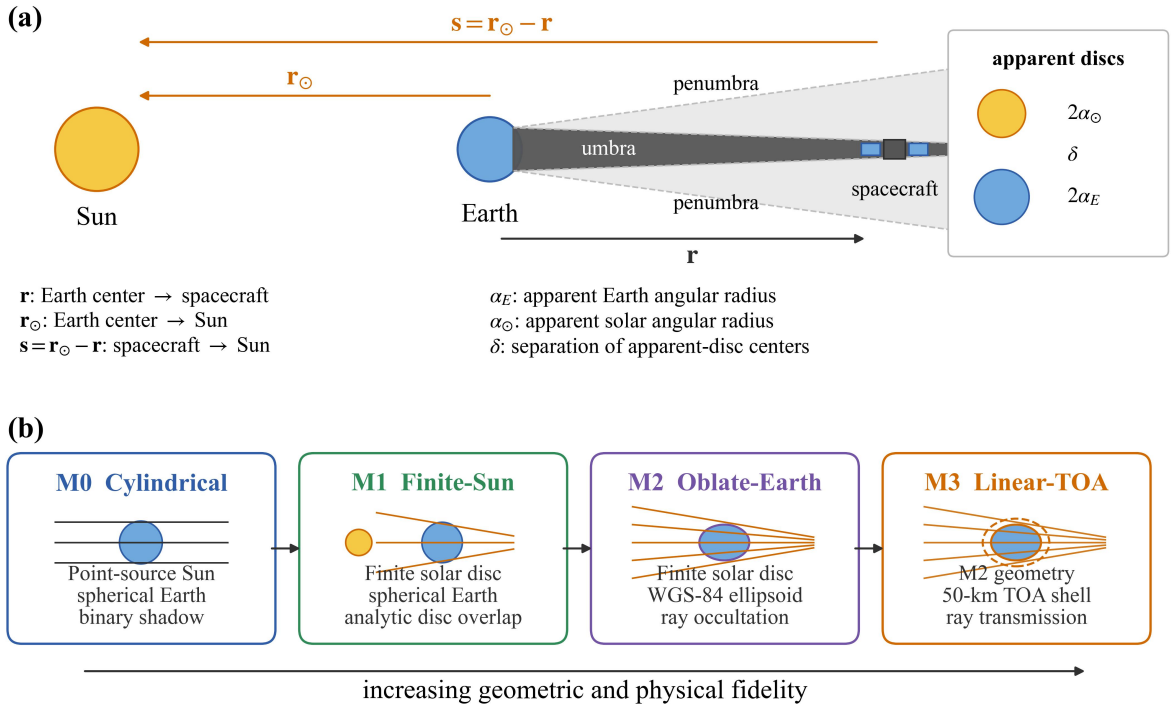


Figure 1: Eclipse geometry and implemented fidelity hierarchy. (a) Geometric vectors and apparent-disc parameters for finite-Sun models. (b) Successive updates from M0 to M3: finite solar size, WGS–84 earth oblateness, and top-of-atmosphere transmission.

M0: cylindrical shadow.

Let $\hat{\mathbf{u}}_\odot = \mathbf{r}_\odot/\|\mathbf{r}_\odot\|$. The axial and transverse coordinates relative to the Sun direction are

$$\xi = \mathbf{r}\cdot\hat{\mathbf{u}}_\odot, \qquad \rho = \|\mathbf{r} - \xi\hat{\mathbf{u}}_\odot\|\,. \tag{2.22}$$

The binary cylindrical factor is Ferraz Mello (1972)

$$\nu_{\mathrm{M0}} = \begin{cases} 0, & \xi < 0 \text{ and } \rho \le a_E, \\ 1, & \text{otherwise.} \end{cases} \tag{2.23}$$

M0 replaces the finite-Sun geometry by parallel rays and a cylindrical switch. Its difference from M1 therefore includes the cylindrical approximation to the shadow boundary as well as the removal of partial illumination.

M1: analytic spherical finite-Sun model.

The apparent angular radii of the Sun and spherical Earth and their angular separation are

$$\alpha_\odot = \sin^{-1}\!\left(\frac{R_\odot}{s}\right), \qquad \alpha_E = \sin^{-1}\!\left(\frac{a_E}{r}\right), \qquad \delta = \cos^{-1}\!\left(\frac{(-\mathbf{r})\cdot\mathbf{s}}{rs}\right). \tag{2.24}$$

For two discs with radii a and b and center separation d, the partial-overlap branch, $|a-b| < d < a+b$, is

$$\begin{aligned} A_\cap(a,b,d) = {} & a^2\cos^{-1}\!\left(\frac{d^2+a^2-b^2}{2da}\right) + b^2\cos^{-1}\!\left(\frac{d^2+b^2-a^2}{2db}\right) \\ & - \frac{1}{2}\sqrt{(-d+a+b)(d+a-b)(d-a+b)(d+a+b)}. \end{aligned} \tag{2.25}$$

The remaining branches are $A_\cap = 0$ for $d \ge a+b$ and $A_\cap = \pi\min(a,b)^2$ for $d \le |a-b|$, including concentric discs. These branches avoid division by zero and include annular occultation. Inverse-trigonometric arguments and the square-root radicand are clipped to their admissible intervals in floating-point evaluation. Angular-disc areas use radians.

The remaining illuminated fraction is then Montenbruck and Gill (2000); Zhang et al. (2022)

$$\nu_{\mathrm{M1}} = \begin{cases} 1, & \delta \ge \alpha_\odot + \alpha_E, \\ 0, & \alpha_E > \alpha_\odot \text{ and } \delta \le \alpha_E - \alpha_\odot, \\ 1 - \dfrac{A_\cap(\alpha_\odot, \alpha_E, \delta)}{\pi\alpha_\odot^2}, & \text{otherwise.} \end{cases} \tag{2.26}$$

The M0–M1 comparison measures replacement of the cylindrical switch by the implemented finite-Sun spherical formulation. M1 assumes uniform solar-disc brightness and excludes atmospheric attenuation. It therefore supplies the analytic spherical comparison against which the later ray-based formulations are evaluated.

M2: ray-integrated oblate-Earth model.

Published oblate-Earth and perspective-projection methods demonstrate the relevance of an ellipsoidal terrestrial limb when eclipse timing and shadow fraction require higher geometric fidelity Adhya et al. (2004); Li et al. (2019); Zhang et al. (2022). M2 evaluates the visibility of the finite solar disc directly against the WGS-84 ellipsoid. A family of ellipsoidal shells is written

$$\mathcal{E}(h): \quad \mathbf{x}^T\mathbf{Q}(h)\mathbf{x} = 1, \qquad \mathbf{Q}(h) = \mathrm{diag}\left(\frac{1}{(a_E+h)^2}, \frac{1}{(a_E+h)^2}, \frac{1}{(b_E+h)^2}\right). \tag{2.27}$$

M2 uses $h = 0$.

The shell coordinate h increases both semi-axes equally and is not geodetic altitude. Consequently, the M3 tangent height is a parameter of these nested shells. To integrate over the apparent solar disc, let $\hat{\mathbf{u}} = \mathbf{s}/s$ and choose orthonormal vectors $\mathbf{e}_1$ and $\mathbf{e}_2$ perpendicular to $\hat{\mathbf{u}}$. The solar angular radius is $\alpha_\odot$. Equal-solid-angle radial nodes are defined by

$$\cos\beta_j = 1 - \frac{j-\frac{1}{2}}{N_r}\left(1-\cos\alpha_\odot\right), \qquad j = 1,\ldots,N_r, \tag{2.28}$$

and azimuthal nodes by

$$\phi_k = \frac{2\pi(k-\frac{1}{2})}{N_\phi}, \qquad k = 1,\ldots,N_\phi. \tag{2.29}$$

The corresponding ray direction is

$$\hat{\mathbf{d}}_{jk} = \hat{\mathbf{u}}\cos\beta_j + (\mathbf{e}_1\cos\phi_k + \mathbf{e}_2\sin\phi_k)\sin\beta_j. \tag{2.30}$$

Uniform solar radiance is assumed; solar limb darkening is not included. The equal-weight rule estimates visible solid angle, whereas M1 uses a planar overlap of angular discs. Their difference can include this representation mismatch as well as finite quadrature error. All transmitted momentum is applied along the solar-centre direction in Eq. (2.13); ray directions determine visibility, not a separately summed vector radiation force. Each ray from the spacecraft is

$$\mathbf{x}_{jk}(\lambda) = \mathbf{r} + \lambda\hat{\mathbf{d}}_{jk}, \qquad \lambda > 0. \tag{2.31}$$

Substitution into Eq. (2.27) gives

$$A_{jk}\lambda^2 + B_{jk}\lambda + C = 0, \tag{2.32}$$

where

$$A_{jk} = \hat{\mathbf{d}}_{jk}^T\mathbf{Q}(0)\hat{\mathbf{d}}_{jk}, \tag{2.33}$$

$$B_{jk} = 2\mathbf{r}^T\mathbf{Q}(0)\hat{\mathbf{d}}_{jk}, \tag{2.34}$$

$$C = \mathbf{r}^T\mathbf{Q}(0)\mathbf{r} - 1. \tag{2.35}$$

A solar-disc ray is occulted when Eq. (2.32) has a positive real intersection between the spacecraft and the Sun. With occultation indicator $I_{jk} = 1$ for a blocked ray and zero otherwise,

$$\nu_{\mathrm{M2}} = 1 - \frac{1}{N_r N_\phi}\sum_{j=1}^{N_r}\sum_{k=1}^{N_\phi} I_{jk}. \tag{2.36}$$

The original production setting uses $N_r = 24$ and $N_\phi = 96$ (2304 solar-disc rays) near eclipse, with bounding-sphere tests outside the transition region. The M1–M2 difference changes both the terrestrial limb and its numerical evaluation. A spherical ray model, denoted M_{1r}, uses the identical ray nodes with $a = b = a_E$ to separate this numerical change from the oblate-limb change in Case 6. This paired evaluation is needed because an analytic-to-ray residual and a change in the projected limb enter the original M1–M2 comparison together.

M3: ray-integrated linear-TOA atmosphere extension.

PPMatm introduces a linear reduction of solar radiation between the solid Earth and a top-of-atmosphere (TOA) ellipsoid, whereas SOLAARS represents substantially richer atmospheric physics Li et al. (2019); Robertson (2015); Zhang et al. (2022). M3 adopts the linear TOA concept but applies it directly to the ray-integrated geometry of M2. It is consequently an atmosphere-aware benchmark model, not a reproduction of PPMatm and not a substitute for SOLAARS-CF. At a common evaluation point, the shared ray directions allow the additional transmission weighting to be distinguished from the binary visibility used by M2.

The TOA shell is $\mathcal{E}(h_{\mathrm{TOA}})$, with baseline $h_{\mathrm{TOA}} = 50$ km. This value is consistent with the practical upper-atmosphere cutoff adopted in the PPMatm development, where interactions above approximately the stratospheric upper boundary were treated as negligible for SRP shadow modeling Li et al. (2019). For each solar-disc ray, three cases are distinguished. A ray intersecting $\mathcal{E}(0)$ has zero transmission. A ray that misses $\mathcal{E}(h_{\mathrm{TOA}})$ has unit transmission. For a ray that intersects the TOA shell but not the solid Earth, the tangent-shell altitude $h^\star_{jk}$ is the smallest shell height for which the ray intersects the inflated ellipsoid,

$$h^\star_{jk} = \inf\left\{h \in [0, h_{\mathrm{TOA}}] : \mathbf{x}_{jk}(\lambda)^T \mathbf{Q}(h) \mathbf{x}_{jk}(\lambda) = 1 \text{ for some } \lambda > 0\right\}. \tag{2.37}$$

This scalar is obtained numerically by bracketing between the solid-Earth and TOA ellipsoids and applying bisection to the ray–ellipsoid intersection condition. Following the linear attenuation structure used in PPMatm, with zero transmission at the solid boundary and unit transmission at the TOA boundary Li et al. (2019); Zhang et al. (2022), M3 assigns

$$\tau_{jk} = \begin{cases} 0, & \text{ray intersects } \mathcal{E}(0), \\ \dfrac{h^\star_{jk}}{h_{\mathrm{TOA}}}, & \text{ray intersects } \mathcal{E}(h_{\mathrm{TOA}}) \text{ but not } \mathcal{E}(0), \\ 1, & \text{ray misses } \mathcal{E}(h_{\mathrm{TOA}}). \end{cases} \tag{2.38}$$

The atmosphere-aware shadow factor is

$$\nu_{\mathrm{M3}} = \frac{1}{N_r N_\phi} \sum_{j=1}^{N_r} \sum_{k=1}^{N_\phi} \tau_{jk}. \tag{2.39}$$

For every solar-disc ray, the M3 transmission does not exceed the corresponding binary visibility used by M2; summation over the common quadrature therefore gives $0 \le \nu_{\mathrm{M3}} \le \nu_{\mathrm{M2}} \le 1$. The linear-TOA atmosphere remains a reduced-order physical assumption; refraction, wavelength dependence, scattering, aerosols, clouds, and solar limb darkening remain outside the present scope.

Radiative-transfer theory distinguishes wavelength-dependent absorption and scattering from a geometric transmission factor Liou (2002). A standard atmospheric profile supplies thermodynamic structure NOAA et al. (1976), while grazing-incidence functions describe slant-path enhancement Vasylyev (2021). None of these ingredients is recovered merely by varying h_{TOA}; the

present height sweep is therefore a model-parameter sensitivity test. No atmospheric parameters are estimated from the propagated trajectory differences in this experiment.

2.4. Numerical verification and internal consistency

Numerical verification comprised independent internal-consistency and resolution-refinement tests designed to characterize two distinct numerical resolution measures. The first is a propagated-position consistency measure associated with time integration and the Encke–Cowell comparison; the second is a pointwise shadow-factor resolution measure associated with solar-disc quadrature. Because these checks are expressed in different metrics, they are interpreted separately rather than combined into a single numerical error floor. Comparisons approaching the relevant resolution level within the corresponding metric are therefore interpreted cautiously rather than assigned independent physical significance. This distinction is important because the successive eclipse formulations differ primarily over the relatively short ingress and egress intervals Oberkampf and Roy (2010).

Unless otherwise stated, the verification calculations used the representative LEO configuration with an altitude of 700 km, inclination $i = 51.6°$, $\Omega = 0°$, $u_0 = 0°$, $A/m = 0.010$ m^2/kg, and $C_R = 1$. The solar state was fixed at the verification epoch $JD_{\mathrm{ver}} = 2460676.5$. Encke–Cowell comparisons were performed over three orbital revolutions using the M3 shadow formulation, whereas the shadow-factor quadrature tests sampled one complete LEO revolution using 4000 uniformly distributed orbital locations. This January geometry is kept separate from the March geometry used for the sensitivity runs.

The recomputed spherical-limit check gives $\max|\nu_{\mathrm{M1}} - \nu_{\mathrm{ray,sph}}| = 2.7571 \times 10^{-3}$ on the specified 4000-point verification grid. This illustrates that a sampled pointwise maximum depends on the test grid. It is not a bound on propagated position error or on other eclipse geometries. The inequality $\nu_{\mathrm{M3}} \leq \nu_{\mathrm{M2}}$ is a separate implementation check implied by the prescribed transmission law.

The propagation implementation was assessed by comparing the regularized Encke formulation with direct Cartesian Cowell integration under the same central-gravity and SRP force model. Both formulations used classical fourth-order Runge–Kutta integration, while the Encke reference trajectory was evaluated from the universal-variable Kepler solution Battin (1999); Curtis (2014); Hairer et al. (1993). Table 2 summarizes the resulting consistency and refinement errors. Agreement between these formulations tests their numerical consistency while leaving the shared physical assumptions unchanged.

Table 2 reports the January-epoch verification output from the common MATLAB implementation. The Encke–Cowell discrepancy decreases from 2.4146×10^{-3} to 1.6476×10^{-4} m between 1200 and 2400 steps/revolution. The Encke 1200-to-2400 difference is 4.6600×10^{-9} m. These observations concern M3 and four sampled checkpoints only; near-roundoff differences do not constitute a practical position-accuracy certificate. They do not establish an equivalent error level for M0, other orbital regimes, or 50-period propagation. The latter limitation is directly demonstrated by the additional LEO results in Table 6.

For M2, the pointwise difference relative to the 4096-ray evaluation is 1.1719×10^{-2} at 1024 rays and 5.2083×10^{-3} at 2304 rays. The corresponding M3 values are 5.7878×10^{-5} and 1.8814×10^{-5}. These are sampled differences between finite quadratures, not errors relative to an exact reference. The smoother prescribed M3 transmission gives smaller differences in this geometry, and Case 6 reports how quadrature changes affect propagated trajectory differences.

The original Cases 1–4 used $N_{\mathrm{step}} = 1200$, local refinement factor eight, $\epsilon_{\mathrm{rect}} = 10^{-3}$, 24×96 rays, and $h_{\mathrm{TOA}} = 50$ km. These settings identify the source of the existing tables and figures.

Table 2: Recomputed numerical checks at $JD_{\mathrm{ver}} = 2460676.5$, LEO 700 km, $i = 51.6°$, and $A/m = 0.010$ m^2 kg^{-1}. Position differences use four checkpoints over three initial periods with M3; shadow-factor differences use 4000 uniform orbital samples.

Numerical check	Metric	Value
M1 analytic vs. spherical ray integration	$\max \lvert\Delta\nu\rvert$	2.7571×10^{-3}
Encke vs. Cowell, 1200 steps/rev	$\max \lVert\Delta\mathbf{r}\rVert$	2.4146×10^{-3} m
Encke vs. Cowell, 2400 steps/rev	$\max \lVert\Delta\mathbf{r}\rVert$	1.6476×10^{-4} m
Encke vs. Cowell, 4800 steps/rev	$\max \lVert\Delta\mathbf{r}\rVert$	3.4622×10^{-5} m
Encke, 300 vs. 2400 steps/rev	$\max \lVert\Delta\mathbf{r}\rVert$	2.4520×10^{-7} m
Encke, 600 vs. 2400 steps/rev	$\max \lVert\Delta\mathbf{r}\rVert$	8.9355×10^{-8} m
Encke, 1200 vs. 2400 steps/rev	$\max \lVert\Delta\mathbf{r}\rVert$	4.6600×10^{-9} m
M2, 1024 vs. 4096 solar rays	$\max \lvert\Delta\nu\rvert$	1.1719×10^{-2}
M2, 2304 vs. 4096 solar rays	$\max \lvert\Delta\nu\rvert$	5.2083×10^{-3}
M3, 1024 vs. 4096 solar rays	$\max \lvert\Delta\nu\rvert$	5.7878×10^{-5}
M3, 2304 vs. 4096 solar rays	$\max \lvert\Delta\nu\rvert$	1.8814×10^{-5}

Their sufficiency for each reported trajectory difference remains subject to the output-level checks in Cases 5 and 6; no general computational-efficiency claim is inferred from the short LEO test. A common nominal resolution does not guarantee a common numerical error across configurations. In particular, the absolute time step grows with orbital period and the binary M0 boundary requires separate treatment. The production and control datasets are therefore distinguished by their initial conditions, integration settings, and output grids. Their comparison tests the interpretation of a reported sensitivity rather than changing the definition of the original experiment.

2.5. Controlled sensitivity cases and discrepancy metrics

The baseline spacecraft parameters are $A/m = 0.010$ m^2 kg^{-1}, $C_R = 1$, $\Omega = 0°$, and $u_0 = 0°$. Four representative circular orbit regimes are used in the area-to-mass and inclination studies (Table 3). The controlled parameter sets are summarized in Table 4, and the common computational architecture is shown in Fig. 2. Each production configuration is propagated with all four shadow formulations so that the adjacent fidelity increments are available throughout the original sweeps. Case 3 uses

$$h\,[\mathrm{km}] = \{400, 700, 1200, 2000, 8000, 13000, 20200, 26000, \\ 31000, 35786, 40000, 50000, 60000, 75000\}. \tag{2.40}$$

Case 4 uses the MEO/GNSS radius and $i = 55°$ so that RAAN remains well defined.

Table 3: Representative circular-orbit regimes.

Regime	Altitude (km)	Baseline inclination
LEO	700	51.6°
MEO/GNSS-radius	20200	55.0°
GEO-radius	35786	0°
High-Earth circular	60000	0°



Figure 2: Computational architecture of the controlled equal-revolution benchmark. The force model, eclipse hierarchy, and production numerical settings remain fixed across the sensitivity sweeps; only the designated orbital or spacecraft parameter varies within each case.

Table 4: Controlled sensitivity design.

	Case 1	Case 2	Case 3	Case 4
Swept parameter	A/m	Inclination	Altitude	RAAN
Range	$\{0.005, 0.010,$ $0.020, 0.050\}$ m^2/kg	$0° : 5° : 180°$	14 altitudes	$0° : 10° : 350°$
Orbit radius	four regimes	four regimes	swept	MEO/GNSS
Inclination	regime baseline	swept	51.6°	55°
RAAN	0°	0°	0°	swept
N_{orb}	0–50	0–50	0–50	0–50
Model pairs	adjacent + M0–M3	adjacent + M0–M3	adjacent + M0–M3	adjacent + M0–M3

For a model pair (M_i, M_j), the sampled position discrepancy is

$$\Delta r_{ij}(N) = \|\mathbf{r}_i(t_N) - \mathbf{r}_j(t_N)\|\,, \tag{2.41}$$

with

$$\Delta r_{\max,ij} = \max_{N=0,\ldots,50} \Delta r_{ij}(N). \tag{2.42}$$

Equation 2.42 is a maximum over 51 checkpoints, not a continuous-time maximum. The supplementary reference solution is also evaluated at 120 samples per initial period, including every original checkpoint. Both maxima are reported from the same reference trajectory, together with signed RTN components in the frame of the first model in each pair.

In the tables, D_{ij} abbreviates $\Delta r_{\max,ij}$. A dense sampled maximum remains a discrete statistic and only bounds from below the continuous-time maximum of that same trajectory. For 30-day runs the checkpoint set comprises complete initial periods and the final endpoint. Comparisons of numerical settings use identical output times; changing the output grid alone does not constitute integration refinement.

The primary decomposition is

$$\{M0 - M1,\ M1 - M2,\ M2 - M3\}, \tag{2.43}$$

while M0–M3 measures the cumulative consequence of traversing the complete implemented hierarchy. During the one-eclipse analysis, the corresponding maximum instantaneous shadow-factor and SRP-acceleration differences are also reported:

$$\Delta\nu_{\max,ij} = \max_t |\nu_i(t) - \nu_j(t)|, \qquad \Delta a_{\text{SRP},\max,ij} = \max_t \|\mathbf{a}_{\text{SRP},i} - \mathbf{a}_{\text{SRP},j}\|. \tag{2.44}$$

For the reported transition results, the maxima in Eq. (2.44) are evaluated on the sampled single-revolution grid, not by continuous extremum detection. The representative transition analysis and the production sensitivity studies use the common fixed solar state at $JD_{\text{sens}} = 2460754.5$. The separate verification state at $JD_{\text{ver}} = 2460676.5$ is confined to Section 2.4.

2.6. Numerical controls and assumption sensitivity

The parameter sweeps establish how the implemented model differences vary with spacecraft and orbital geometry. Their interpretation requires two further distinctions: a change in physical assumptions must be separated from a change in numerical evaluation, and an equal-period

comparison must be distinguished from a common elapsed-time comparison. Cases 5–8 address these questions using the same production epoch, $C_R = 1$, and $u_0 = 0$. The main article selects comparisons that answer these questions directly; Supplementary Tables 1–11 retain all settings, numerical flags, and sampling records.

Temporal control (Case 5) uses seven configurations spanning the LEO baseline, inclined MEO and GEO-radius orbits, the 60000 and 75000 km altitude range, a high-area-to-mass equatorial orbit, and the MEO orientation $\Omega = 350°$. Each configuration is integrated for 50 initial periods at 1200, 2400, and 4800 nominal RK4 steps per period. An adaptive Encke-deviation comparison uses the variable-order Adams solver `ode113` Shampine and Reichelt (1997) with a maximum step $T_0/1200$. Relative tolerances are 10^{-11} and 10^{-13}, with position absolute tolerances 10^{-8} and 10^{-10} m and velocity absolute tolerances 10^{-11} and 10^{-13} m s^{-1}. M0 integration is split at cylindrical-shadow events, followed by a 1 μs smooth-arc restart. The shared force and shadow functions make this an integration comparison rather than independent validation of the physical model.

For $\mathbf{d}_{ij} = \mathbf{r}_i - \mathbf{r}_j$, numerical agreement is evaluated on common nominal-period checkpoints through the vector change E and scalar-maximum change S:

$$E_{ij}^{h,h/2} = \max_N \|\mathbf{d}_{ij}^{h}(t_N) - \mathbf{d}_{ij}^{h/2}(t_N)\|, \qquad S_{ij}^{h,h/2} = |\Delta r_{\max,ij}^{h} - \Delta r_{\max,ij}^{h/2}|. \tag{2.45}$$

On an identical sample set, the reverse triangle inequality gives

$$S_{ij}^{h,h/2} \le E_{ij}^{h,h/2}, \qquad D_{03} \le D_{01} + D_{12} + D_{23}. \tag{2.46}$$

The second relation follows from $\mathbf{d}_{03} = \mathbf{d}_{01} + \mathbf{d}_{12} + \mathbf{d}_{23}$ at each epoch. Neither inequality supplies an error bound relative to the exact trajectory: both compare computed histories. Superscripts on E and S may also denote two ray grids or adaptive tolerances.

The reporting screen is $E \le 0.001\,\mathrm{m} + 0.01 D^{(b)}$, where $D^{(b)}$ is the comparison solution's checkpoint maximum. The 1 mm absolute term and 1 percent relative term define a reporting convention, not a mission requirement or an absolute orbit-error bound. Passing one comparison is insufficient to establish convergence; the focused verification therefore reports successive refinements and the available formulation comparison. Its stricter diagnostic screen also applies the same threshold to each individual trajectory; these state checks are reported separately from pair-vector stability, and failed checks are not relabelled as passes. Adaptive output additionally includes 120 samples per initial period; whenever its dense maximum is reported, that convention is stated explicitly. A smaller adaptive value is not, by itself, evidence of greater accuracy.

Geometric evaluation is controlled separately in Case 6 by using a spherical ray model M_{1r} with the same nodes as M2. Grids of 2304, 4096, and 9216 rays are compared at 4800 steps per period for LEO, an equatorial 60000 km orbit, and MEO at $\Omega = 350°$. Thus M1–M_{1r} measures the analytic-to-ray residual, while M_{1r}–M2 changes the limb at matched nodes. Case 8 complements temporal control by sampling neighboring altitudes and low inclinations around the original high-altitude feature.

Finally, Case 7 changes the assumptions that determine eclipse exposure: frozen versus evolving solar geometry and 50 periods versus 30 days. All four baseline regimes are retained at 4800 steps per period and 2304 rays. A separate LEO/MEO comparison varies the linear transmission height from 25 to 75 km, holding the numerical refinement envelope at 75 km. These tests describe sensitivity to the adopted experiment; they do not introduce additional operational force models or calibrate an atmosphere.

3. Results and Discussion

3.1. From eclipse geometry to the applied perturbation

The representative 700 km LEO passage links the shadow geometry to the forcing used in the subsequent propagation study. It uses $i = 51.6°$, $\Omega = u_0 = 0$, $A/m = 0.010$ m^2/kg, and the production near-equinox solar state. Figure 3 shows that the models differ primarily at ingress and egress, while Table 5 distinguishes a displacement of the transition from a change in its duration. The common geometry permits these transition changes to be examined before their accumulated trajectory consequences are considered.

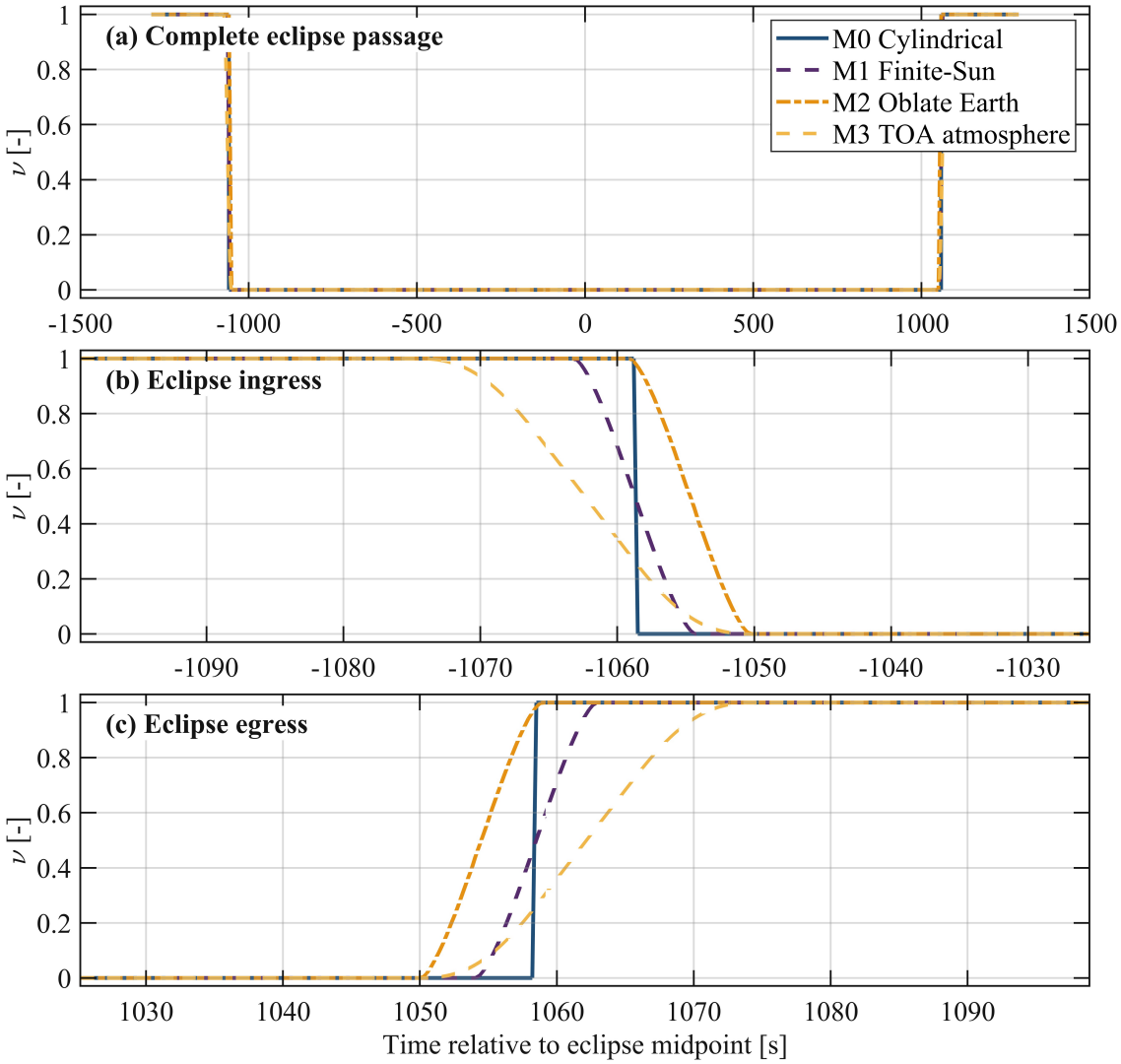


Figure 3: Shadow-factor profiles for the representative LEO eclipse passage: (a) complete eclipse, (b) ingress, and (c) egress. M0 represents the binary cylindrical formulation, M1 the analytic finite-Sun spherical-Earth model, M2 the finite-Sun WGS–84 oblate-Earth ray-integration model, and M3 the ray-wise linear top-of-atmosphere extension.

Finite solar size replaces the M0 switch with an approximately nine-second M1 penumbra. M2 shifts the transition epochs by about four seconds relative to M1, with comparatively little change in duration. The prescribed M3 transmission instead broadens ingress and egress to approximately 23 seconds, because rays that miss the solid Earth can remain partially attenuated. The reported 0.29633 s M0 egress interval reflects threshold sampling, not a physical penumbra.

Table 5: Eclipse-transition epochs for the representative LEO shadow analysis. Times are measured from the beginning of the sampled orbital revolution. The thresholds $\nu = 10^{-3}$ and $\nu = 1 - 10^{-3}$ distinguish deep eclipse, partial attenuation, and full illumination.

Model	Enter pen. (s)	Enter umb. (s)	Exit umb. (s)	Exit pen. (s)	Ingress (s)	Egress (s)
M0	1899.5	1899.5	4016.2	4016.5	0	0.29633
M1	1895.1	1903.6	4012.1	4021.0	8.5937	8.8900
M2	1899.2	1907.8	4007.9	4017.1	8.5937	9.1863
M3	1884.4	1906.9	4008.8	4031.6	22.521	22.818

For this passage, the adjacent illumination-factor maxima are 0.49862, 0.56197, and 0.72193, and the cumulative maximum is 0.73712. Their corresponding acceleration differences are 2.2930×10^{-8}, 2.5843×10^{-8}, 3.3199×10^{-8}, and 3.3897×10^{-8} m s^{-2}, respectively. The M3–M2 inequality is satisfied throughout the sampled passage. An analytic-to-spherical-ray residual of 3.08324×10^{-3} is smaller than the instantaneous M1–M2 separation in this geometry. These local observations explain how the forcing changes, but neither this ordering nor this residual determines the long-horizon orbit difference. That distinction motivates the temporal comparison below.

3.2. Temporal resolution of the propagated differences

A physical interpretation of the parameter sweeps first requires their numerical scale to be established. Table 6 isolates time-step dependence in the 50-period LEO baseline. The cumulative maximum changes nonmonotonically from 0.208185 to 0.035268 and 0.159135 m. The associated pair-vector changes are 0.191181 and 0.142131 m, showing that the variation is not merely a shift of the maximizing epoch.

Table 6: Completed 50-period LEO RK4 refinement subset. Entries are sampled position differences in metres, not absolute orbit errors.

Steps/period	M0–M1	M1–M2	M2–M3	M0–M3
1200	0.104705	0.146956	0.250437	0.208185
2400	0.086256	0.147977	0.251238	0.035268
4800	0.055833	0.148628	0.251931	0.159135

Table 7 extends this comparison to every Case 5 configuration while retaining a common checkpoint metric. The high-area-to-mass equatorial result changes from about 80.16 m to 17.82 m between the selected RK4 settings, whereas the tighter adaptive checkpoint value is about 27.98 m. None of the seven M0–M1 adaptive tolerance comparisons satisfies the selected screen. M1–M2 and M2–M3 satisfy that tolerance screen in six and seven configurations, respectively, although this does not establish joint temporal and ray-grid convergence.

Sampling introduces a distinct difference. At 75000 km, the tighter adaptive M0–M3 maximum is 1.70306 m at checkpoints and 2.15032 m on dense output. The adaptive column in Table 7 therefore uses checkpoint values, not the exported dense maxima. The complete sampling and refinement records are retained in the supplement. With this numerical context established, the following figures and original tables can be read as conditional sensitivity maps at the production settings, rather than as absolute error estimates.

Table 7: Case 5: cumulative M0–M3 checkpoint maxima at 1200 and 4800 RK4 steps per period and at the tighter adaptive setting (AT). The last column gives the M0–M1 pair-vector change between adaptive tolerances. All distances are in metres; all runs use 50 periods and $A/m = 0.01$ m^2/kg, except the equatorial 60000 km row, which uses 0.05 m^2/kg.

h (km)	i (deg)	Ω (deg)	R1200	R4800	AT	E_{01}^{tol}
700	51.6	0	0.2082	0.1591	0.1046	0.0019
20200	55	0	3.0963	0.2925	0.1622	0.0059
35786	51.6	0	9.4329	2.3212	0.5009	0.0199
60000	51.6	0	23.5333	5.5763	1.1899	0.0223
60000	0	0	80.1597	17.8187	27.9825	0.0365
75000	51.6	0	16.9449	9.3203	1.7031	0.0245
20200	55	350	8.5488	9.5137	9.5225	0.0077

The focused verification uses 23 paired runs in two frozen-Sun configurations at the production epoch: L=(700 km, 51.6°, 0°, 0.01 m^2/kg) and H=(60000 km, 0°, 0°, 0.05 m^2/kg), where entries specify altitude, inclination, RAAN, and area-to-mass ratio. Both span 50 initial periods and compare M0 with M1; no ray quadrature enters this pair. Twelve runs are available for L and eleven for H, including one independently stepped Cowell calculation for L. RK4 is evaluated at 4800, 9600, and 19200 nominal steps per period, retaining the production eclipse-refinement rule. Event-split Encke integration uses `ode113`, relative tolerance 10^{-13}, and successive maximum steps $T_0/1200$, $T_0/2400$, $T_0/4800$, and $T_0/9600$. The final setting is denoted J and remains a comparison solution rather than an exact reference.

M0 contacts are located as events and the illuminated and shadowed arcs are integrated separately. Additional calculations reduce the restart advance from 10^{-6} to 10^{-8} s, deliberately delay switching by those intervals, and reduce the relative tolerance to 3×10^{-14}. The deliberate delay tests measure response to a displaced switch; they are not an event-location tolerance. The Encke position and velocity absolute tolerances are 10^{-10} m and 10^{-13} m/s at the nominal relative tolerance. The Cowell formulation uses dimensionless Cartesian position and velocity with component absolute tolerances 10^{-15}, retaining the same force and shadow laws but selecting integration steps independently. Consequently, their agreement tests equation representation and numerical integration, not independent physical validity.

Table 8 shows why the pair response and individual states must be interpreted separately. In L, the J maximum is 1.28754 mm, and the final two Encke pair-vector changes are 6.14×10^{-5} and 4.51×10^{-5} mm. The independently stepped Cowell result changes the pair vector by 0.0237 mm, about 1.84% of the J maximum, whereas the larger individual-state change is 18.6 mm. This pattern is consistent with substantial cancellation of a shared numerical displacement when the model difference is formed; it does not establish that the common displacement is physically correct. The strict state-based screen therefore remains unsatisfied, although the available comparisons support reporting a differential response of approximately 1.3 mm. The finest RK4 pair vector still differs from J by 5.09 mm, so the older production value is not interchangeable with the event-split estimate.

In H, the J maximum is 1.06364 m, compared with 1.78210 m at the finest RK4 setting. The RK4-to-J pair-vector change is 0.71849 m, whereas the successive final Encke changes are 0.0198 and 0.1519 mm. The latter sequence is nonmonotonic and does not establish an asymptotic convergence order. Moreover, the final individual-state change reaches 0.1743 m, and no H Cowell

Table 8: Focused M0–M1 verification over 50 initial periods. All distances are in metres. D is the checkpoint maximum, E is the maximum pair-vector change, and e_{state} is the larger of the two individual-trajectory changes on identical checkpoints. L and H are defined in the text.

Quantity or comparison	L	H
RK4, 9600 steps: D	0.01523023	3.236243
RK4, 19200 steps: D	0.003806837	1.782101
Event-split J: D	0.00128754	1.063639
E: $T_0/1200$ to $T_0/2400$	1.081×10^{-7}	7.730×10^{-5}
E: $T_0/2400$ to $T_0/4800$	6.137×10^{-8}	1.983×10^{-5}
E: $T_0/4800$ to J	4.507×10^{-8}	0.0001519379
E: finest RK4 to J	0.005094349	0.7184912
e_{state}: $T_0/4800$ to J	2.926×10^{-5}	0.1743218
E: J to Cowell	2.373×10^{-5}	n/a
e_{state}: J to Cowell	0.01860274	n/a

n/a denotes a formulation comparison not included in the available H subset. The stricter individual-state screen is not satisfied for all comparisons in either configuration; the table does not certify absolute accuracy.

comparison is included in this subset. The evidence supports an approximately 1.064 m response within the tested event-split Encke family, with an explicit formulation limitation rather than an unconditional accuracy claim. This M0–M1 value must not be substituted for the cumulative M0–M3 values in Table 7.

Every compared event-split M0 history contains 100 contacts, and the maximum contact-time changes across the time refinements through J are approximately 7.33×10^{-9} s for L and 6.93×10^{-5} s for H. Restart, deliberate-delay, and tolerance tests change the pair vectors by no more than approximately 1.85×10^{-6} m and 2.12×10^{-5} m, respectively, within the available controls. Maxima sampled at 120, 240, and 480 points per initial period from each J trajectory equal its checkpoint maximum to the exported precision. This sampling result applies only to these two histories and does not imply that checkpoint maxima are sufficient for all geometries. The full numerical comparisons are retained in the supplement, including failed individual-state screens and the distinction between missing and completed formulation checks. These controls establish a bounded interpretation of differential sensitivity without extending the result to the untested ray-based pairs or to all production extrema.

3.3. Area-to-mass-ratio sensitivity and fidelity decomposition

Case 1 quantifies the sensitivity of the propagated shadow-model discrepancies to spacecraft area-to-mass ratio across the four prescribed circular-orbit regimes. The tested values were $\frac{A}{m} = \{0.005,\ 0.010,\ 0.020,\ 0.050\}\ \mathrm{m^2\,kg^{-1}}$. For each value of A/m, the remaining spacecraft and numerical parameters were held fixed at $C_R = 1$, $\Omega = 0°$, and $u_0 = 0°$. The production calculations used the common solar geometry at $JD_{\text{sens}} = 2460754.5$, corresponding to a Sun–Earth distance of 1.489651×10^{11} m and the inertial solar unit vector $\hat{\mathbf{u}}_{\odot} = \begin{bmatrix} 0.99997967 & -0.00585029 & -0.00253593 \end{bmatrix}^{\mathrm{T}}$. The reference epoch was selected near the equinox so that all four prescribed orbital planes encounter the terrestrial shadow under the common baseline orientation. This provides a consistent eclipse-conditioned geometry for comparing the sensitivity of the different orbital regimes without changing the Sun state between cases.

All Case 1 trajectories were propagated to $N_{\mathrm{orb}} = 50$ with the original common settings: 1200 nominal steps per revolution, local refinement factor eight, $\epsilon_{\mathrm{rect}} = 10^{-3}$, and 24×96 rays. These settings identify the original area-to-mass-ratio sweep; the LEO refinement results above show that they do not establish numerical qualification for every model pair. Figures 4 and 5 retain the original production output. M0–M1 compares cylindrical and finite-Sun spherical formulations; M1–M2 also changes numerical evaluation and therefore needs the spherical-ray control in Case 6. M2–M3 applies the prescribed atmospheric transmission. These comparisons are conditional model differences, not separately validated physical error components.

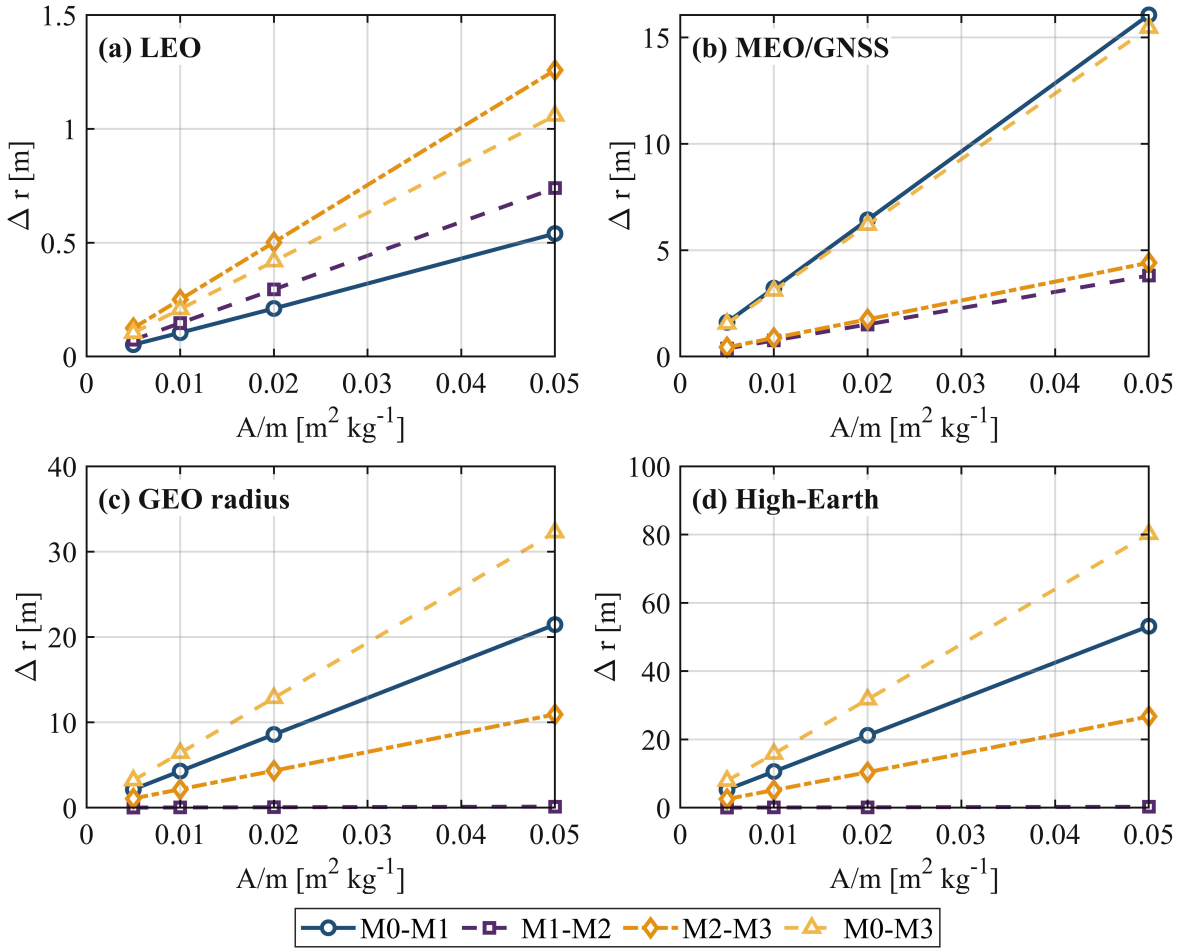


Figure 4: Case 1 maximum propagated discrepancy as a function of area-to-mass ratio across the four orbit regimes. Model increments: solar size (M0–M1), Earth oblateness (M1–M2), and atmospheric attenuation (M2–M3); M0–M3 represents the cumulative discrepancy.

The maximum discrepancies extracted from the trajectories are reported in Table 9. The selected near-equinox geometry yields eclipse encounters in all four prescribed regimes, producing non-zero model-pair discrepancies and enabling a common cross-regime comparison. The approximately proportional response to A/m in Figs. 4 and 5 is consistent with the linear factor in the cannonball acceleration. Over the tenfold range, the LEO M2–M3 separation changes from 0.12511 to 1.2573 m, while the High-Earth M0–M1 separation changes from 5.2981 to 53.152 m. These examples establish the scale of the computed response without implying that its integration error scales independently of A/m.

The relative size of the increments also changes with geometry. At the baseline area-to-mass ratio, the largest adjacent separation is M2–M3 in LEO but M0–M1 in several higher-orbit pro-

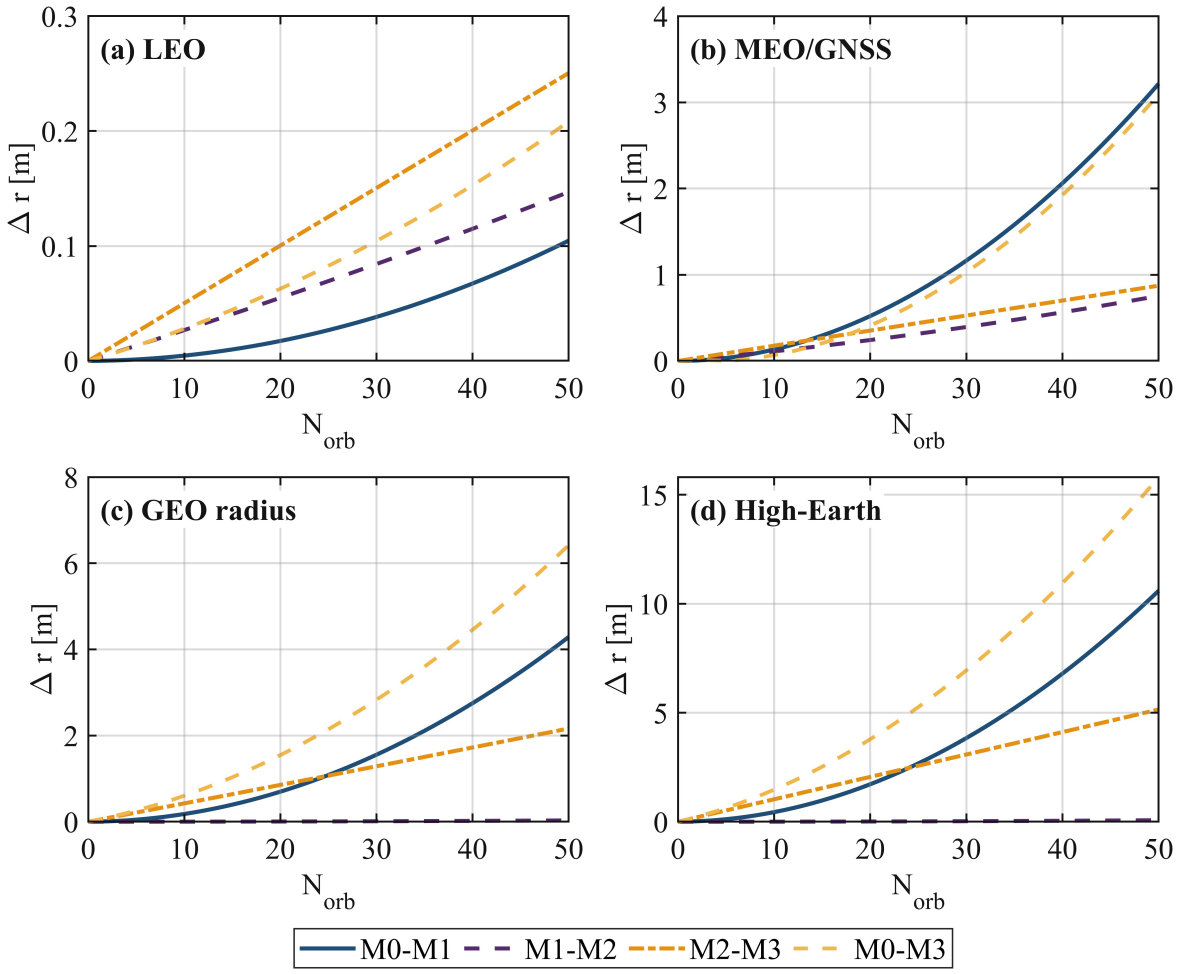


Figure 5: Case 1 discrepancy accumulation over nominal revolution index N_{orb} at $A/m = 0.010$ m^2 kg^{-1} across the four orbit regimes.

Table 9: Case 1 maximum propagated position discrepancies over $N_{\mathrm{orb}} = 0, \ldots, 50$ for the tested area-to-mass ratios.

Regime	A/m (m^2/kg)	M0–M1 (m)	M1–M2 (m)	M2–M3 (m)	M0–M3 (m)
LEO	0.005	0.052148	0.073379	0.12511	0.10388
LEO	0.010	0.10470	0.14696	0.25044	0.20818
LEO	0.020	0.21105	0.29455	0.50156	0.41804
LEO	0.050	0.53988	0.73949	1.2573	1.0577
MEO/GNSS	0.005	1.6077	0.37717	0.43641	1.5485
MEO/GNSS	0.010	3.2150	0.75479	0.87352	3.0963
MEO/GNSS	0.020	6.4286	1.5117	1.7501	6.1901
MEO/GNSS	0.050	16.058	3.8059	4.4098	15.455
GEO-radius	0.005	2.1440	0.015655	1.0800	3.2084
GEO-radius	0.010	4.2877	0.030413	2.1629	6.4202
GEO-radius	0.020	8.5750	0.056222	4.3364	12.855
GEO-radius	0.050	21.451	0.12558	10.939	32.264
High-Earth	0.005	5.2981	0.034448	2.5619	7.8944
High-Earth	0.010	10.595	0.068977	5.1470	15.810
High-Earth	0.020	21.191	0.12443	10.400	31.716
High-Earth	0.050	53.152	0.27309	26.735	80.160

duction runs. Meanwhile, M1–M2 is appreciable in inclined LEO and MEO but small in the equatorial GEO-radius and High-Earth cases. Because these comparisons change orbital-plane geometry as well as radius, the results do not isolate altitude as the cause of that ordering. The matched-ray control below addresses the additional evaluation change within M1–M2.

The largest cumulative production value, 80.160 m, occurs at $A/m = 0.050$ m^2/kg in High-Earth orbit. Its magnitude must be interpreted together with the temporal dependence in Table 7. Likewise, the coherent growth visible in the accumulation histories depends on repeated eclipse phase and on elapsed time: fifty periods represent about 3.43 days in LEO and 98.49 days in High-Earth orbit. Equal nominal periods thus organize the experiment without equating its physical duration.

Finally, the adjacent maximum norms are not additive. In the LEO baseline their sum is 0.50210 m, whereas the cumulative maximum is 0.20818 m. The underlying vectors add at a common epoch, but their norms can peak at different times and in different directions. This explains why neither a local illumination ranking nor a sum of adjacent maxima predicts the cumulative trajectory separation.

A dynamical explanation follows from the specific orbital energy, $\mathcal{H}_k = v_k^2/2 - \mu_E/r_k$. Under Eq. (2.12),

$$\frac{d}{dt}(\mathcal{H}_i - \mathcal{H}_j) = \mathbf{v}_i \cdot \mathbf{a}_{\mathrm{SRP},i} - \mathbf{v}_j \cdot \mathbf{a}_{\mathrm{SRP},j}. \tag{3.1}$$

Illumination differences act through signed orbital work, so ingress and egress contributions can reinforce or cancel. For nearby bound orbits, the osculating semi-major-axis difference satisfies $\Delta a \simeq 2a_0^2 \Delta\mathcal{H}/\mu_E$, giving $\Delta n \simeq -3n\Delta a/(2a_0)$ to first order. Persistent energy differences can therefore produce along-track phase drift, whereas oscillatory work need not produce secular growth. The explicit factor A/m explains a leading-order proportional response when trajectory and contact shifts remain small; it does not imply exact linearity of eclipse-crossing trajectories.

3.4. Sensitivity to orbital-plane orientation

Case 2 examines the sensitivity of the propagated shadow-model discrepancies to orbital inclination while retaining the same eclipse-conditioned solar geometry used for the production sensitivity studies. The inclination was varied over

$$i = 0^\circ : 5^\circ : 180^\circ, \tag{3.2}$$

for each of the four circular orbit regimes. The remaining quantities were fixed at their baseline values: $A/m = 0.010$ m^2 kg^{-1}, $C_R = 1$, $\Omega = 0^\circ$, and $u_0 = 0^\circ$. The solar state was fixed at $JD_{\mathrm{sens}} = 2460754.5$ throughout the sweep. At the endpoint inclinations $i = 0^\circ$ and 180°, the assigned value $\Omega = 0^\circ$ follows the Cartesian-state convention defined in Section 2.1.

All Case 2 trajectories were propagated to $N_{\mathrm{orb}} = 50$ using the same original settings: 1200 nominal RK4 steps per revolution, refinement factor eight, $\epsilon_{\mathrm{rect}} = 10^{-3}$, and 24×96 rays. Holding these settings fixed does not remove configuration-dependent numerical error; local extrema in the inclination sweep therefore require the additional checks described above. Figure 6 shows the resulting inclination sensitivity. The response is strongly non-monotonic for the M0–M1 and cumulative M0–M3 comparisons, whereas the M2–M3 atmospheric increment varies much more smoothly with inclination within each orbital regime. Selected inclination values are reported in Table 10.

Figure 6 and Table 10 show that the prescribed inclination response is nonmonotone, particularly for M0–M1 and M0–M3. Changing inclination changes both the apparent limb and the

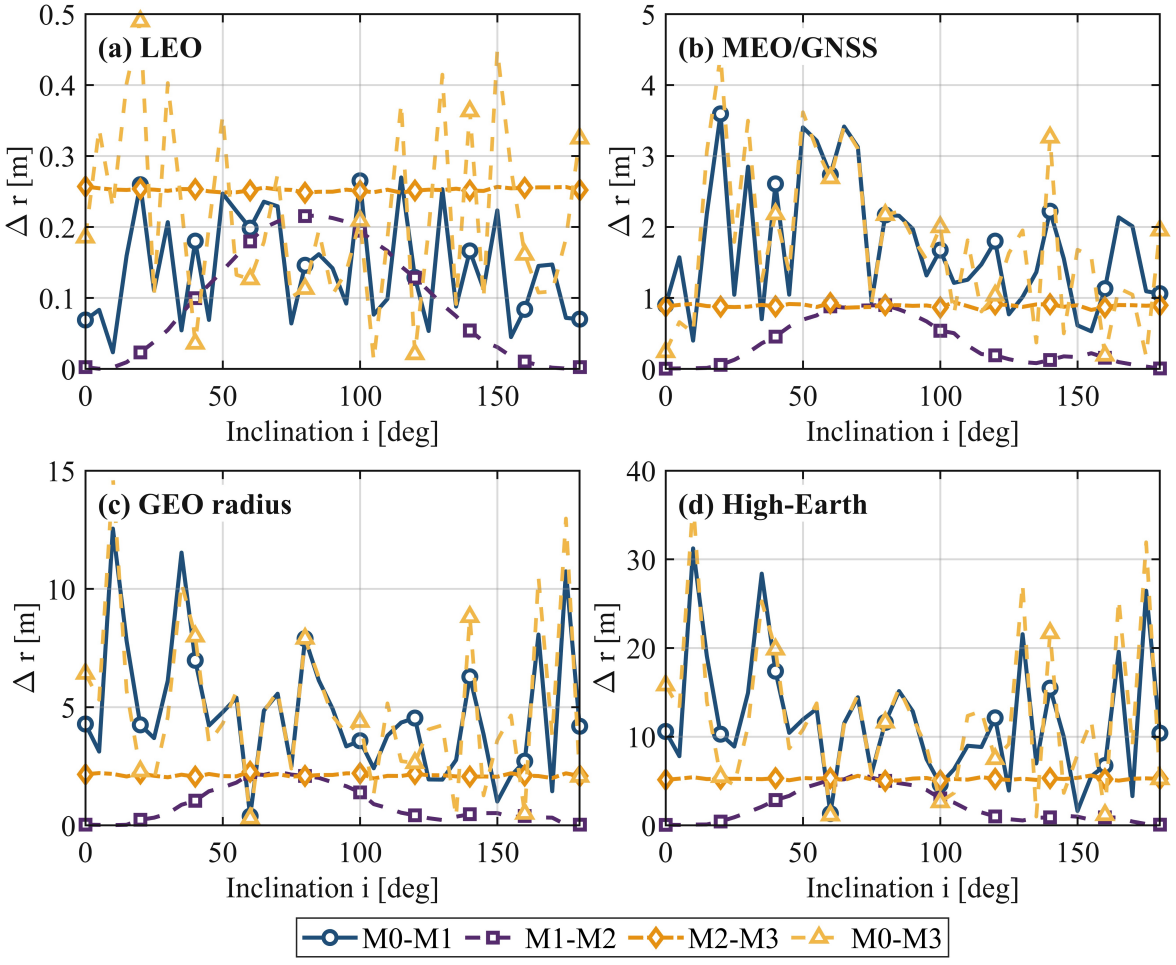


Figure 6: Case 2 sensitivity of adjacent fidelity increments and cumulative M0–M3 discrepancy to orbital inclination across the four orbit regimes under fixed production solar geometry.

Table 10: Selected Case 2 maximum propagated position discrepancies for the inclination sweep. Each value is the maximum over $N_{\mathrm{orb}} = 0, \ldots, 50$.

Regime	i (deg)	M0–M1 (m)	M1–M2 (m)	M2–M3 (m)	M0–M3 (m)
LEO	0	0.069032	0.002545	0.25695	0.18538
LEO	30	0.20678	0.054979	0.25099	0.40279
LEO	55	0.22232	0.15922	0.24896	0.13258
LEO	90	0.14192	0.21260	0.24970	0.10482
LEO	120	0.12887	0.12862	0.25133	0.021087
LEO	150	0.22335	0.030888	0.25656	0.44902
LEO	180	0.070245	0.002626	0.25197	0.32484
MEO/GNSS	0	0.89893	0.006165	0.88094	0.23917
MEO/GNSS	30	2.8497	0.22987	0.87813	3.4979
MEO/GNSS	55	3.2150	0.75479	0.87352	3.0963
MEO/GNSS	90	1.9737	0.76438	0.88948	1.8486
MEO/GNSS	120	1.8009	0.19182	0.91144	1.0358
MEO/GNSS	150	0.61450	0.16752	0.89862	1.6806
MEO/GNSS	180	1.0611	0.006605	0.89901	1.9535
GEO-radius	0	4.2877	0.030413	2.1629	6.4202
GEO-radius	30	6.1230	0.50119	2.0355	4.5888
GEO-radius	55	5.3988	1.8121	2.0764	5.6630
GEO-radius	90	4.9380	1.8246	2.1345	4.6281
GEO-radius	120	4.5397	0.42996	2.1803	2.6424
GEO-radius	150	1.0106	0.52217	2.0592	3.5919
GEO-radius	180	4.1927	0.034402	2.0926	2.0657
High-Earth	0	10.595	0.068977	5.1470	15.810
High-Earth	30	14.941	1.4861	5.2443	11.183
High-Earth	55	13.144	4.6565	5.2848	13.772
High-Earth	90	12.870	4.5289	5.2827	12.116
High-Earth	120	12.130	1.0113	5.2508	7.5023
High-Earth	150	1.6321	0.98603	5.3634	7.9815
High-Earth	180	10.405	0.078241	5.2532	5.2297

phase of eclipse forcing. It also changes how the transition is sampled by the integration scheme. The temporal results therefore prevent a sharp peak in this figure from being identified directly with a physical resonance.

The comparatively small M1–M2 differences near the equatorial limits contrast with the larger values at inclined orientations. This pattern is consistent with the direction-dependent projected limb, but M1–M2 also changes from analytic to ray evaluation. The spherical-ray control in Section 3.7 is consequently needed to judge whether the evaluation residual is small relative to the inferred limb increment. The smoother M2–M3 curve describes the response of the prescribed transmission law; its smoothness is not evidence of atmospheric validation. The inclination sweep therefore identifies geometries requiring closer examination rather than establishing a single preferred model. Case 8 returns to the low-inclination high-altitude configurations after the altitude response has been considered, allowing the neighboring values to be compared under altered integration settings.

3.5. Altitude sensitivity under equal-revolution normalization

Case 3 evaluates the sensitivity of the propagated model discrepancies to orbital altitude while preserving the equal-revolution benchmark definition. The inclination was fixed at $i = 51.6°$, with $\Omega = 0°$, $u_0 = 0°$, $A/m = 0.010$ m^2 kg^{-1}, and $C_R = 1$. The solar geometry was held fixed at the production epoch $JD_{\mathrm{sens}} = 2460754.5$, and each case was propagated to $N_{\mathrm{orb}} = 50$, corresponding to 50 nominal initial-orbit periods, using the common production settings: 1200 nominal RK4 steps per revolution, an eclipse refinement factor of eight, the Encke rectification threshold $\epsilon_{\mathrm{rect}} = 10^{-3}$, and a 24×96 solar-disc quadrature corresponding to 2304 rays. The sweep therefore changes orbital radius while retaining a common initial orbital-plane orientation.

The altitude sweep contains 14 circular-orbit altitudes ranging from 400 km to 75,000 km. Because the propagation horizon is defined by a fixed nominal revolution index rather than by a fixed elapsed time, the physical duration represented by the benchmark increases with orbital period. Thus, Case 3 isolates an equal-nominal-revolution response, while explicitly retaining the fact that higher orbits accumulate the model differences over a longer physical time interval. Figure 7 shows the resulting maximum propagated discrepancies as functions of altitude, and the corresponding numerical values are summarized in Table 11.

The altitude response in Fig. 7 and Table 11 combines changing eclipse geometry with increasing elapsed time. M2–M3 is the largest adjacent separation in the low-altitude production runs, whereas M0–M1 becomes larger over much of the medium- and high-altitude range. Beyond GEO radius, the M1–M2 and M2–M3 curves are relatively smooth, while M0–M1 exhibits pronounced local structure. These observations describe the computed curves; they do not establish a universal physical hierarchy.

The 60000 km production configuration gives M0–M1 and M0–M3 maxima of 24.476 and 23.533 m, respectively. Selecting neighboring points is more informative than treating this isolated peak as an optimum. Table 12 therefore brackets it with the 55000 and 65000 km cases and retains all three low-inclination tests at 60000 km. The complete nine-configuration Case 8 dataset remains in the supplement; the selection here is based on proximity to the feature, not on whether a numerical screen is satisfied.

The large production values change substantially with integration setting: at $i = 10°$, for example, the reported maximum changes from approximately 31.2330 m to 2.1237 m between the RK4 settings. Adaptive values are smaller, but the complete Case 8 vector comparisons do not satisfy the selected screen. Thus the added data delimit the interpretation of the original peak rather than replacing it with a new physical optimum. A separate question remains: how much

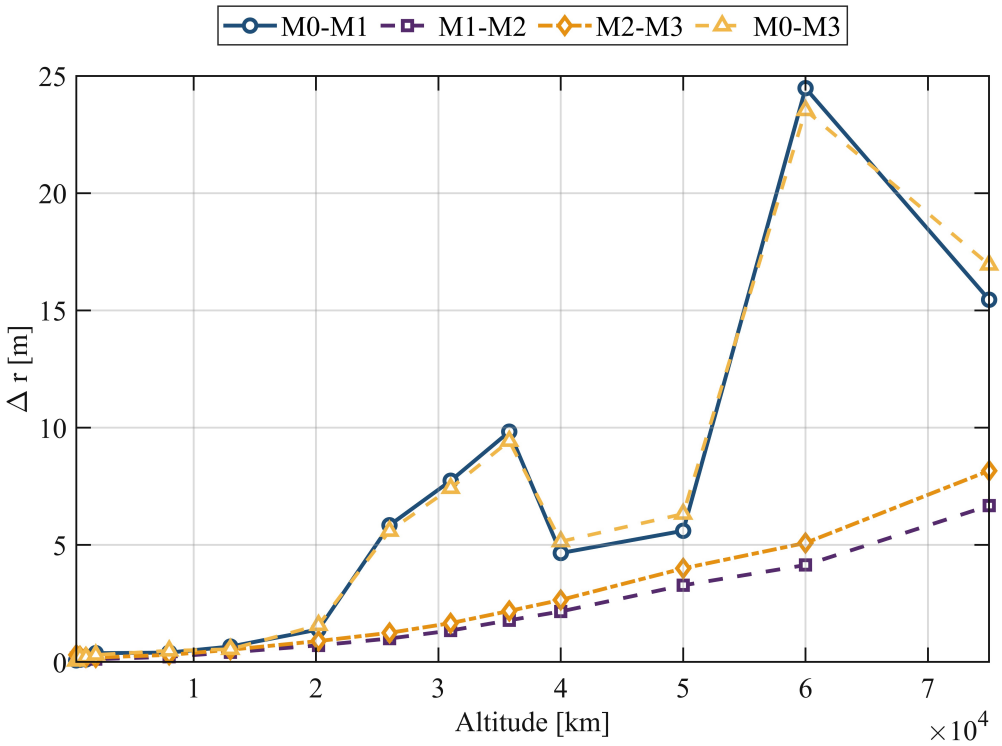


Figure 7: Maximum propagated position discrepancy versus altitude for the adjacent fidelity increments and the cumulative M0–M3 comparison. The propagation horizon is fixed at $N_{\mathrm{orb}} = 50$, corresponding to 50 initial Keplerian periods, for every altitude.

Table 11: Case 3 altitude sweep under equal-revolution normalization. Each discrepancy is the maximum over $N_{\mathrm{orb}} = 0, \ldots, 50$.

Altitude (km)	Period (h)	50-rev time (days)	M0–M1 (m)	M1–M2 (m)	M2–M3 (m)	M0–M3 (m)
400	1.5427	3.2139	0.079191	0.17846	0.31251	0.059056
700	1.6462	3.4296	0.10470	0.14696	0.25044	0.20818
1200	1.8237	3.7994	0.11924	0.13222	0.21537	0.20240
2000	2.1200	4.4166	0.38560	0.13018	0.20199	0.31379
8000	4.7661	9.9294	0.41017	0.22996	0.31192	0.49212
13000	7.4572	15.536	0.66696	0.41983	0.53181	0.55499
20200	11.978	24.955	1.3967	0.71894	0.90255	1.5803
26000	16.106	33.554	5.8403	1.0092	1.2534	5.5962
31000	19.977	41.619	7.7380	1.3505	1.6659	7.4226
35786	23.934	49.863	9.8300	1.7887	2.1859	9.4329
40000	27.611	57.522	4.6555	2.1643	2.6569	5.1480
50000	37.006	77.096	5.6035	3.2796	3.9991	6.3230
60000	47.277	98.493	24.476	4.1432	5.0865	23.533
75000	64.176	133.70	15.456	6.6749	8.1646	16.945

Table 12: Case 8: selected M0–M1 maxima (m) bracketing the 60000 km altitude feature and covering the complete low-inclination subset. R columns use checkpoints; AT reports dense adaptive output. All use 50 periods, a frozen Sun, $\Omega = 0$, and $A/m = 0.01$ m^2/kg.

Altitude (km)	i (deg)	R1200	R4800	AT
55000	51.6	20.7239	4.1489	0.1871
60000	51.6	24.4764	4.6061	0.2062
65000	51.6	10.0626	0.9290	0.2192
60000	5	7.8094	3.6538	0.2063
60000	10	31.2330	2.1237	0.2067
60000	15	19.1094	0.9261	0.2067

of the broad altitude response is associated with the longer duration represented by fifty periods? The common-duration comparison in Section 3.8 addresses that issue.

3.6. RAAN sensitivity at the MEO/GNSS radius

Case 4 examines the dependence of the propagated shadow-model discrepancies on the right ascension of the ascending node (RAAN). The semi-major axis was fixed at the MEO/GNSS reference radius, corresponding to an altitude of 20,200 km, while the inclination was fixed at $i = 55°$. The RAAN was varied over

$$\Omega = 0° : 10° : 350°. \tag{3.3}$$

The other parameters retained their production values: $A/m = 0.010$ m^2 kg^{-1}, $C_R = 1$, and $u_0 = 0°$. The solar geometry was fixed at $JD_{\text{sens}} = 2460754.5$.

Each RAAN configuration was propagated to $N_{\text{orb}} = 50$, corresponding to 50 nominal initial-orbit periods, using 1200 nominal RK4 steps per revolution, an eclipse refinement factor of eight, $\epsilon_{\text{rect}} = 10^{-3}$, and a 24×96 solar-disc quadrature corresponding to 2304 rays. Thus, the RAAN sweep changes only the orientation of the orbital plane relative to the prescribed Sun direction. Figure 8 shows a strongly localized RAAN response. Broad ranges of node orientation produce zero model-to-model discrepancy, whereas relatively narrow RAAN intervals generate pronounced peaks. This behavior is consistent with eclipse exposure under the fixed solar geometry; the zero sampled differences alone do not establish an eclipse-free trajectory. Selected numerical values from the RAAN sweep are summarized in Table 13.

For a circular orbit and the cylindrical parallel-ray approximation, a geometric eclipse is possible when $a_0|\sin\beta| < a_E$, where $\beta = \sin^{-1}(\hat{\mathbf{h}} \cdot \hat{\mathbf{u}}_\odot)$ and $\hat{\mathbf{h}}$ is the orbit-normal unit vector. Thus both i and Ω control access to shadow through the solar beta angle. Finite solar size, oblateness, and subsequent orbital evolution modify the contacts; this criterion explains localization qualitatively rather than predicting the amplitudes of the propagated peaks. Its role is to identify access to the shadow region, while the propagated response must still be assessed from the time-dependent forcing.

The asymmetric sampled response also shows why eclipse exposure must be interpreted with the specified epoch and initial phase. The cumulative production values at $\Omega = 0°$ and $180°$ are 3.0963 and 0.33575 m, respectively, so the frequent zero values do not establish a global $180°$ symmetry. The directed Sun vector and fixed initial argument of latitude distinguish these configurations. The large M1–M2 response near $\Omega = 350°$ further shows why orbital-plane orientation must

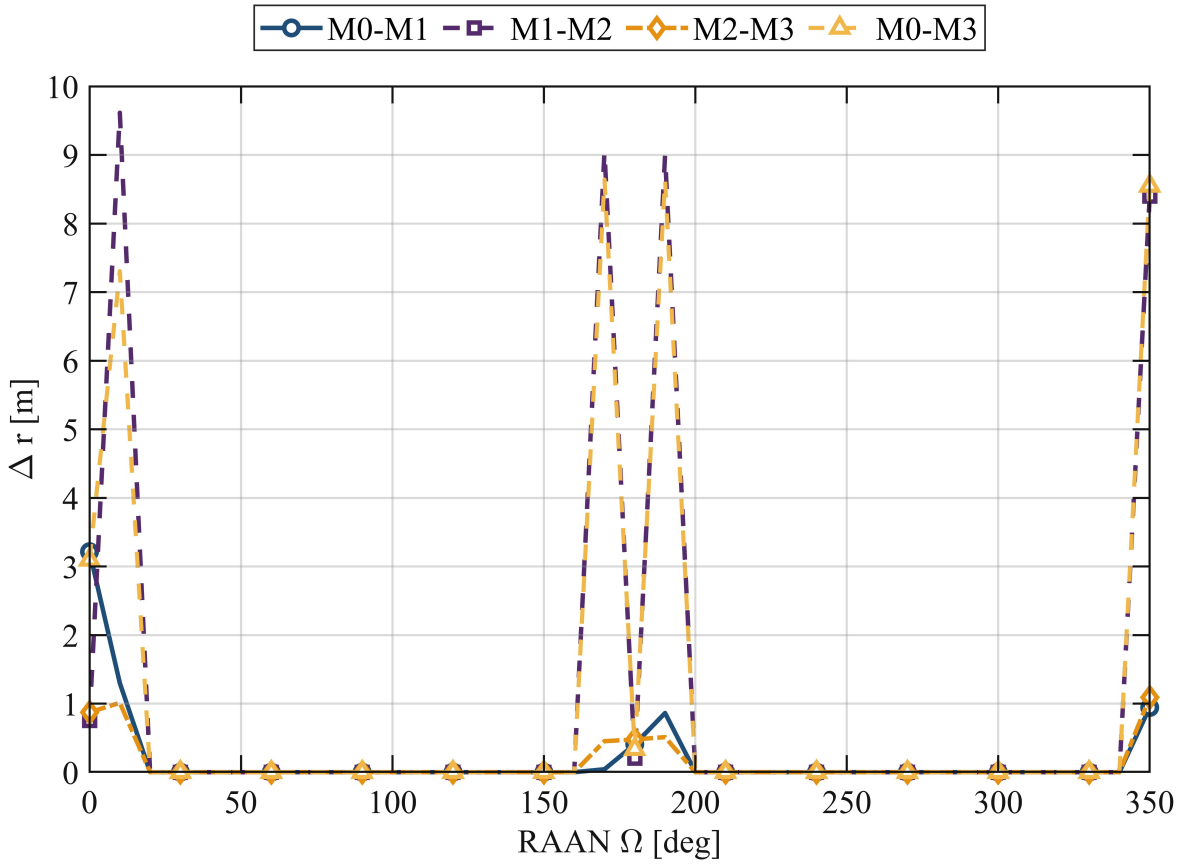


Figure 8: Case 4 sensitivity of adjacent fidelity increments and cumulative M0–M3 discrepancy to RAAN sweep at MEO/GNSS radius ($i = 55°$) under fixed production solar geometry.

Table 13: Selected Case 4 maximum propagated position discrepancies at the MEO/GNSS radius with $i = 55°$. Each value is the maximum over $N_{\mathrm{orb}} = 0, \ldots, 50$.

Ω (deg)	M0–M1 (m)	M1–M2 (m)	M2–M3 (m)	M0–M3 (m)
0	3.2150	0.75479	0.87352	3.0963
60	0	0	0	0
120	0	0	0	0
180	0.40714	0.20437	0.47753	0.33575
240	0	0	0	0
300	0	0	0	0
350	0.94342	8.4013	1.0911	8.5488

accompany altitude when the limb effect is discussed. This orientation is therefore retained in the matched-ray experiment, which tests the evaluation contribution before the original curve is given a geometric interpretation.

3.7. Separating limb geometry from numerical evaluation

The previous inclination and RAAN results motivate a direct control on M1–M2. Table 14 reports all three Case 6 geometries at the finest ray grid, alongside the changes from the preceding grid. This keeps the central distinction visible without repeating every coarse-grid value: M1–M_{1r} changes the angular representation and numerical evaluation, while M_{1r}–M2 changes the limb at matched nodes. The M2–M3 column retains the corresponding transmission comparison under the same numerical setting.

Table 14: Case 6: finest-grid checkpoint maxima (9216 rays) and changes from 4096 to 9216 rays, at 4800 steps per period. All distances are in metres. The three geometries are $(h\,[\mathrm{km}], i, \Omega) = (700, 51.6^\circ, 0)$, $(60000, 0, 0)$, and $(20200, 55^\circ, 350^\circ)$; $A/m = 0.01$ m^2/kg throughout.

Geometry	$D_{1,1r}$	$D_{1r,2}$	D_{23}	E_{12}	S_{12}
LEO	0.0002	0.1484	0.2515	0.0002	0.0002
High, equatorial	0.0059	0.0165	5.2209	0.0438	0.0011
MEO, node 350	0.0046	8.4210	1.0763	0.0033	0.0033

The evaluation residual is small relative to the larger limb-related separation in the inclined LEO and MEO examples, but it is not negligible in the equatorial High-Earth case. In that case, the analytic-to-spherical-ray maximum is 0.0059 m and the matched-limb maximum is 0.0165 m, so the evaluation change cannot be ignored when interpreting the analytic-to-oblate comparison. More importantly, grid refinement changes the M1–M2 scalar maximum by about 0.0011 m but its pair-vector history by about 0.0438 m, exceeding the finest-grid M1–M2 maximum of about 0.0225 m. This is a concrete instance in which an apparently stable scalar summary fails to describe the stability of the propagated difference. The matched-node control therefore improves attribution, while the vector diagnostic prevents that attribution from being mistaken for a completed joint time-and-ray convergence assessment.

3.8. Dependence on solar evolution and propagation duration

The remaining assumption concerns the time over which the geometry is allowed to evolve. Table 15 retains all four regimes and both horizons but focuses on M1–M2 and M2–M3, which directly connect the limb and transmission questions to the preceding analysis. The M0-related outputs and all other Case 7 metrics remain in the supplement. This choice avoids presenting the already unresolved binary-shadow contribution as the principal measure of solar-evolution sensitivity.

There is no uniform frozen-to-moving correction in these computations. Over thirty days in LEO, the M1–M2 output increases from about 2.50 to 33.16 m, whereas the High-Earth M2–M3 output over fifty periods decreases from about 5.17 to 1.17 m. The opposite changes show that the prescribed solar history can alter both the scale and apparent relative importance of model differences at the selected numerical settings. An altitude or model ranking obtained with equal periods and a frozen Sun therefore cannot be transferred directly to an equal-duration moving-Sun experiment. Because these runs have no dedicated temporal-refinement series, their contribution

Table 15: Case 7: checkpoint maxima (m) under frozen (F) and moving (M) solar geometry, at 4800 steps per period and 2304 rays. The regimes are $(700, 51.6°)$, $(20200, 55°)$, $(35786, 0°)$, and $(60000, 0°)$ in altitude (km) and inclination. All use $\Omega = 0$ and $A/m = 0.01$ m^2/kg.

Regime	Horizon	D_{12} F	D_{12} M	D_{23} F	D_{23} M
LEO	50 periods	0.1486	0.0953	0.2519	0.2515
LEO	30 days	2.5002	33.1621	2.2632	2.1847
MEO	50 periods	0.7745	4.2499	0.8960	1.0714
MEO	30 days	0.9930	6.9173	1.0774	1.5253
GEO-radius	50 periods	0.0216	0.6335	2.1079	1.5414
GEO-radius	30 days	0.0083	0.6378	1.2666	1.5227
High	50 periods	0.0213	0.4622	5.1729	1.1743
High	30 days	0.0018	0.4622	1.5450	1.1492

is to demonstrate sensitivity to the comparison protocol, not to establish validated correction magnitudes.

Table 16 isolates a narrower modelling choice by retaining every tested transmission height. The near-proportional LEO and MEO response over 25–75 km is consistent with sensitivity to the prescribed linear law. Holding the numerical refinement envelope fixed prevents this particular input change from simultaneously moving the step-refinement trigger. The result characterizes the adopted transmission prescription and does not select a physically calibrated atmospheric boundary.

Table 16: Case 7: M2–M3 checkpoint maxima (m) for three transmission heights, at 50 periods with a frozen Sun. The ray grid and step count match Table 15; the numerical refinement envelope is fixed at 75 km.

Height (km)	LEO	MEO
25	0.1252	0.4513
50	0.2519	0.8960
75	0.3805	1.3408

3.9. Implications for interpreting eclipse-model sensitivity

The combined results identify three distinct quantities that an eclipse-model comparison must keep separate: a change in the shadow prescription, a change in the computed trajectory, and a change in the reported summary of that trajectory. The matched-ray experiment addresses the first distinction by holding the evaluation nodes fixed while changing the limb. The focused Encke/RK4/Cowell comparisons address the second by separating differential stability from individual-state agreement. The vector-versus-scalar and horizon controls address the third by showing how apparently similar maxima or nominal durations can conceal different histories. The contribution is therefore a linked set of quantitative attribution tests, illustrated by counterexamples in the benchmark, rather than an additional parameter sweep or a new shadow law.

For practical interpretation, a reported eclipse-model separation should identify the model pair, initial state, solar history, elapsed horizon, and output sampling, together with the numerical changes relevant to that pair. A scalar maximum can summarize the result, but the vector-history

change is needed to determine whether that summary is stable under refinement. When the comparison changes an analytic evaluation into a ray-based one, the matched spherical-ray residual provides a separate measure of the evaluation change before the limb contribution is discussed. When the intended use concerns a differential response, that response and individual-state changes should both be reported, rather than allowing cancellation to imply absolute accuracy. These requirements turn the benchmark findings into a reporting procedure that can be applied to other eclipse-model comparisons without assuming that the present numerical magnitudes transfer to other missions.

The available evidence does not include a refined comparison of integrated SRP work with the final specific-energy change for the oblate and atmospheric pairs. Illumination differences and elapsed time therefore provide physical context, but cannot by themselves establish the sign or magnitude of the accumulated along-track response. A longer attenuation interval can contribute differently depending on orbital phase and the direction of the SRP acceleration relative to velocity. Table 17 distinguishes the contributions supported by the computed records from these broader physical interpretations. This scope preserves the quantitative findings while avoiding a claim of a demonstrated orbital-work mechanism or complete numerical qualification of the sensitivity maps.

Table 17: Evidence supporting the interpretation of the benchmark and the associated limits.

Question	Available evidence	Supported interpretation and limit
M0–M1 sensitivity	23 paired runs; two geometries; one Cowell comparison	Conditional differential estimates; individual-state qualification remains incomplete.
Production extrema	RK4 refinement and event-split comparisons	Numerical dependence is demonstrated; original maxima are not physical correction bounds.
Oblate-limb contribution	Case 6 matched spherical and oblate rays	Separates limb and evaluation changes at tested settings; no global joint convergence claim.
Solar and horizon effects	Case 7 frozen/moving Sun and two horizons	Dependence on the prescribed geometry and duration; no general seasonal or operational prediction.
Atmospheric increment	Case 7 transmission-height comparisons	Sensitivity to the linear law; neither atmospheric calibration nor a verified orbital-work mechanism.

Atmospheric realism is a separate evidential question. Published atmospheric models have been compared with accelerometer or orbit-determination data Robertson et al. (2015); Li et al. (2019); Zhang et al. (2022); changing a linear transmission height cannot provide equivalent validation. The present M3 results quantify sensitivity to a chosen transmission law. Likewise, the restriction to initially circular states, central gravity, cannonball SRP, and approximate solar geometry excludes conclusions about operational orbit accuracy, resonant structure, or general eccentric-orbit behavior. Additional force models or seasonal and phase ensembles become necessary if those broader claims are pursued; they are not required to define the present restricted benchmark.

4. Conclusion

This study establishes a controlled comparison of eclipse-model sensitivity and numerical effects for initially circular Earth orbits under central gravity and cannonball SRP. Its contribution is to combine matched geometric evaluation, common-checkpoint vector diagnostics, and controlled solar and horizon variations when interpreting propagated model differences. The original sweeps map the response to spacecraft loading and orbital geometry, while supplementary controls reveal which features depend on the definition and numerical realization of the experiment. In particular, the equatorial matched-ray case changes its scalar maximum by only 0.0011 m while its pair-vector history changes by 0.0438 m, demonstrating that scalar agreement alone can conceal instability. The benchmark thus supplies specific evidence for reporting vector-history changes alongside the familiar maximum separation.

The 23-run focused verification further distinguishes differential stability from agreement of the individual trajectories. Event-split Encke propagation gives cylindrical-to-finite-Sun maxima of approximately 1.288 mm in LEO and 1.064 m in the selected high Earth orbit, compared with 3.807 mm and 1.782 m at the finest tested RK4 settings. The available LEO Cowell comparison changes the pair vector by about 0.024 mm while the individual trajectories change by about 18.6 mm, illustrating the importance of reporting both quantities. Small differential changes therefore support configuration-specific comparisons but do not establish absolute orbit accuracy; the nonmonotonic high-orbit refinement and incomplete individual-state qualification remain explicit limits. Likewise, the original 80.160 m cumulative production maximum cannot be adopted as a verified physical correction magnitude. The useful result is the identification and quantification of these distinctions, rather than selection of a preferred value solely because it is smaller.

Matched spherical-ray controls show how to distinguish evaluation changes from the occulting-limb change at the tested settings, while frozen/moving-Sun and equal-period/equal-duration controls demonstrate dependence on the comparison protocol. Transmission-height results quantify sensitivity to the prescribed linear law without calibrating an atmosphere. Together, these findings support a reproducible reporting procedure in which a model-pair maximum is accompanied by its geometric, temporal, sampling, and numerical context. The evidence does not establish a quantitative orbital-work mechanism or global joint convergence of the ray-based survey, and the conclusions are bounded accordingly. Applying the same controls to additional force models, eccentric orbits, and observation-based validation would test transferability beyond the present idealized benchmark. Within its stated scope, the study provides quantitative diagnostics for assessing when an eclipse-model difference can be interpreted and when its numerical origin remains significant.

Declaration of Generative AI and AI-assisted Technologies in the Writing Process

During the preparation of this work, the author used ChatGPT to improve the clarity and academic language of the manuscript. The author reviewed and edited the content as needed and takes full responsibility for the final version of the manuscript.

Competing interests

The author declares no financial or non-financial competing interests relevant to this work.

Research funding

This research received no external funding.

Data availability

The full data for Cases 5–8 and the focused verification cases are provided in the supplementary material.

References

Adhya, S., Sibthorpe, A., Ziebart, M., Cross, P., 2004. Oblate Earth eclipse state algorithm for low-earth-orbiting satellites. Journal of Spacecraft and Rockets 41, 157–159. doi:10.2514/1.1485.

Alessi, E.M., Colombo, C., Rossi, A., 2019. Phase space description of the dynamics due to the coupled effect of the planetary oblateness and the solar radiation pressure perturbations. Celestial Mechanics and Dynamical Astronomy 131, 43. doi:10.1007/s10569-019-9919-z.

Arnold, D., Meindl, M., Beutler, G., Dach, R., Schaer, S., Lutz, S., Prange, L., Sośnica, K., Mervart, L., Jäggi, A., 2015. CODE's new solar radiation pressure model for GNSS orbit determination. Journal of Geodesy 89, 775–791. doi:10.1007/s00190-015-0814-4.

Battin, R.H., 1999. An Introduction to the Mathematics and Methods of Astrodynamics. AIAA Education Series. revised ed., American Institute of Aeronautics and Astronautics, Reston, VA.

Bhattarai, S., Ziebart, M., Allgeier, S., Grey, S., Springer, T., Harrison, D., Li, Z., 2019. Demonstrating developments in high-fidelity analytical radiation force modelling methods for spacecraft with a new model for GPS IIR/IIR-M. Journal of Geodesy 93, 1515–1528. doi:10.1007/s00190-019-01265-7.

Chen, X., Ge, M., Männel, B., Hugentobler, U., Schuh, H., 2024. Extending higher-order model for non-conservative perturbing forces acting on Galileo satellites during eclipse periods. Journal of Geodesy 98, 113. doi:10.1007/s00190-024-01924-4.

Curtis, H.D., 2014. Orbital Mechanics for Engineering Students. 3rd ed., Elsevier/Butterworth-Heinemann, Oxford, UK.

Duan, B., Hugentobler, U., 2021. Enhanced solar radiation pressure model for GPS satellites considering various physical effects. GPS Solutions 25, 42. doi:10.1007/s10291-020-01073-z.

Duan, B., Hugentobler, U., Hofacker, M., Selmke, I., 2020. Improving solar radiation pressure modeling for GLONASS satellites. Journal of Geodesy 94, 72. doi:10.1007/s00190-020-01400-9.

Duan, B., Hugentobler, U., Selmke, I., Marz, S., Killian, M., Rott, M., 2022. BeiDou satellite radiation force models for precise orbit determination and geodetic applications. IEEE Transactions on Aerospace and Electronic Systems 58, 2823–2836. doi:10.1109/TAES.2021.3140018.

Ferraz Mello, S., 1972. Analytical study of the Earth's shadowing effects on satellite orbits. Celestial Mechanics 5, 80–101. doi:10.1007/BF01227825.

Fliegel, H.F., Gallini, T.E., Swift, E.R., 1992. Global positioning system radiation force model for geodetic applications. Journal of Geophysical Research: Solid Earth 97, 559–568. doi:10.1029/91JB02564.

Gkolias, I., Alessi, E.M., Colombo, C., 2020. Dynamical taxonomy of the coupled solar radiation pressure and oblateness problem and analytical deorbiting configurations. Celestial Mechanics and Dynamical Astronomy 132, 55. doi:10.1007/s10569-020-09992-2.

Hairer, E., Nørsett, S.P., Wanner, G., 1993. Solving Ordinary Differential Equations I: Nonstiff Problems. volume 8 of *Springer Series in Computational Mathematics*. 2nd revised ed., Springer, Berlin, Germany.

Hubaux, C., Lemaître, A., Delsate, N., Carletti, T., 2012. Symplectic integration of space debris motion considering several Earth's shadowing models. Advances in Space Research 49, 1472–1486. doi:10.1016/j.asr.2012.02.009.

Li, Z., Ziebart, M., Bhattarai, S., Harrison, D., 2019. A shadow function model based on perspective projection and atmospheric effect for satellites in eclipse. Advances in Space Research 63, 1347–1359. doi:10.1016/j.asr.2018.10.027.

Liou, K.N., 2002. An Introduction to Atmospheric Radiation. volume 84 of *International Geophysics Series*. 2nd ed., Academic Press, San Diego, CA.

McMahon, J.W., Scheeres, D.J., 2010. New solar radiation pressure force model for navigation. Journal of Guidance, Control, and Dynamics 33, 1418–1428. doi:10.2514/1.48434.

Montenbruck, O., Gill, E., 2000. Satellite Orbits: Models, Methods and Applications. Springer, Berlin, Germany. doi:10.1007/978-3-642-58351-3.

Musen, P., 1960. The influence of the solar radiation pressure on the motion of an artificial satellite. Journal of Geophysical Research 65, 1391–1396. doi:10.1029/JZ065i005p01391.

NOAA, NASA, USAF, 1976. U.S. Standard Atmosphere, 1976. Technical Report NOAA-S/T 76-1562. U.S. Government Printing Office. Washington, DC.

Nugnes, M., Colombo, C., 2023. Analytical determination of eclipse entry and exit points considering a conical shadow and oblate Earth. Acta Astronautica 211, 795–807. doi:10.1016/j.actaastro.2023.07.007.

Oberkampf, W.L., Roy, C.J., 2010. Verification and Validation in Scientific Computing. Cambridge University Press, Cambridge, UK. doi:10.1017/CBO9780511760396.

Prša, A., Harmanec, P., Torres, G., Mamajek, E., Asplund, M., Capitaine, N., Christensen-Dalsgaard, J., Depagne, É., Haberreiter, M., Hekker, S., Hilton, J., Kopp, G., Kostov, V., Kurtz, D.W., Laskar, J., Mason, B.D., Milone, E.F., Montgomery, M., Richards, M., Schmutz, W., Schou, J., Stewart, S.G., 2016. Nominal values for selected solar and planetary quantities: IAU 2015 resolution B3. The Astronomical Journal 152, 41. doi:10.3847/0004-6256/152/2/41.

Robertson, R., Flury, J., Bandikova, T., Schilling, M., 2015. Highly physical penumbra solar radiation pressure modeling with atmospheric effects. Celestial Mechanics and Dynamical Astronomy 123, 169–202. doi:10.1007/s10569-015-9637-0.

Robertson, R.V., 2015. Highly Physical Solar Radiation Pressure Modeling During Penumbra Transitions. Ph.D. thesis. Virginia Polytechnic Institute and State University. Blacksburg, VA.

Rodriguez-Solano, C.J., Hugentobler, U., Steigenberger, P., 2012. Adjustable box-wing model for solar radiation pressure impacting GPS satellites. Advances in Space Research 49, 1113–1128. doi:10.1016/j.asr.2012.01.016.

Shampine, L.F., Reichelt, M.W., 1997. The MATLAB ODE suite. SIAM Journal on Scientific Computing 18, 1–22. doi:10.1137/S1064827594276424.

Srivastava, V.K., Ashutosh, A., Roopa, M.V., Ramakrishna, B.N., Pitchaimani, M., Chandrasekhar, B.S., 2014. Spherical and oblate Earth conical shadow models for LEO satellites: Applications and comparisons with real time data and STK to IRS satellites. Aerospace Science and Technology 33, 135–144. doi:10.1016/j.ast.2014.01.010.

Srivastava, V.K., Mishra, P., Ramakrishna, B.N., Kushvah, B.S., 2021. Orbit prediction and Earth shadow modeling for Chandrayaan-2 orbiter. Astrophysics and Space Science 366, 85. doi:10.1007/s10509-021-03991-x.

Srivastava, V.K., Yadav, S.M., Ashutosh, Kumar, J., Kushvah, B.S., Ramakrishna, B.N., Ekambram, P., 2015. Earth conical shadow modeling for LEO satellite using reference frame transformation technique: A comparative study with existing earth conical shadow models. Astronomy and Computing 9, 34–39. doi:10.1016/j.ascom.2014.10.001.

U.S. Naval Observatory, n.d. Computing approximate solar coordinates. Astronomical Applications Department, U.S. Naval Observatory. URL: https://aa.usno.navy.mil/faq/sun_approx. accessed 9 September 2026.

Valk, S., Lemaître, A., 2008. Semi-analytical investigations of high area-to-mass ratio geosynchronous space debris including Earth's shadowing effects. Advances in Space Research 42, 1429–1443. doi:10.1016/j.asr.2008.02.010.

Vallado, D.A., 2013. Fundamentals of Astrodynamics and Applications. 4th ed., Microcosm Press/Springer, Hawthorne, CA.

Vasylyev, D., 2021. Accurate analytic approximation for the Chapman grazing incidence function. Earth, Planets and Space 73, 112. doi:10.1186/s40623-021-01435-y.

Vielberg, K., Peter, H., Kusche, J., Löcher, A., 2025. Updated radiation pressure force modeling and validation: Case studies for GRACE and Sentinel-6 MF. Journal of Geodesy 99, 79. doi:10.1007/s00190-025-02000-1.

Zhang, Y., Wang, X., Xi, K., Li, Z., 2022. Comparison of shadow models and their impact on precise orbit determination of BeiDou satellites during eclipsing phases. Earth, Planets and Space 74, 126. doi:10.1186/s40623-022-01684-5.

Ziebart, M., 2004. Generalized analytical solar radiation pressure modeling algorithm for spacecraft of complex shape. Journal of Spacecraft and Rockets 41, 840–848. doi:10.2514/1.13097.

Supplementary Files

This is a list of supplementary files associated with this preprint. Click to download.

- SupplementaryCases58.pdf